

draft of March 2, 2009

Synthetic Observations of Simulated Radio Galaxies I: Radio and X-ray Analysis

I. L. Tregillis ¹, T. W. Jones ², Dongsu Ryu ³

ABSTRACT

We present an extensive synthetic observational analysis of numerically-simulated radio galaxies designed to explore the effectiveness of conventional observational analyses at recovering physical source properties. These are the first numerical simulations with sufficient physical detail to allow such a study. The present paper focuses on extraction of magnetic field properties from non-thermal intensity information. Synchrotron and inverse-Compton intensities were effective in providing meaningful information about distributions and strengths of magnetic fields, although considerable care was called for in quantitative usage of the information. Correlations between radio and X-ray surface brightness correctly revealed useful dynamical relationships between particles and fields, for example. Magnetic field strength estimates derived from the ratio of X-ray to radio intensity were mostly within about a factor of two of the RMS field strength along a given line of sight. When emissions along a given line of sight were dominated by regions close to the minimum energy/equipartition condition, the field strengths derived from the standard power-law-spectrum minimum energy calculation were also reasonably close to actual field strengths, except when spectral aging was evident. Otherwise, biases in the minimum-energy magnetic field estimation mirrored actual differences from equipartition. The ratio of the inverse-Compton-estimated magnetic field to the minimum-energy magnetic field provided a rough measure of the actual total energy in particles and fields in most instances, although this measure was accurate within only about an order

¹Applied Physics Division, MS B259, Los Alamos National Laboratory, Los Alamos, NM, 87545; iant@lanl.gov

²School of Physics and Astronomy, University of Minnesota, Minneapolis, MN 55455; twj@msi.umn.edu

³Department of Astronomy & Space Science, Chungnam National University, Daejeon, 305-764 Korea; ryu@canopus.chungnam.ac.kr

of magnitude. This may provide a practical limit to the accuracy with which one may be able to establish the internal energy density or pressure of optically thin synchrotron sources.

Subject headings: galaxies: jets — MHD — radiation mechanisms: nonthermal
— radio continuum: galaxies

1. INTRODUCTION

The synchrotron emission from extragalactic radio sources is a function of both the local magnetic fields and the relativistic particle populations residing within. These two components are important to the energy budget of such objects. So, pinning down their relative contributions is crucial to understanding their overall behavior. Unfortunately, the optically-thin synchrotron emission alone cannot be used to extract the individual particle and field components. However, it has long been known that in principle radio synchrotron observations can be combined with X-ray observations of inverse-Compton scattered cosmic microwave background photons (hereafter IC/3K) to extract information about particles and fields in emission regions (e.g., Harris & Romanishin 1974; Cooke et al. 1978; Fabbiano et al. 1979; Harris & Grindlay 1979). The advent of the Chandra and XMM-Newton observatories has made this kind of analysis possible for a large number of classes and objects.

X-ray emission has now been detected in the jets, hotspots, and lobes of numerous radio galaxies and attributed to a host of different physical processes ranging from synchrotron emission (e.g., Wilson et al. (2001)) to inverse Compton scattered emission off of one or more of several photon fields. Brunetti et al. (1999) and Setti et al. (2002) reported the detection of X-ray emission in the lobes of 3C 219 and in 3C 215 and 3C 334 respectively, that possibly arises from inverse-Compton scattering of IR photons from the quasar nucleus. IC/3K lobe emission has been reported in several radio galaxies, including Fornax A (Kaneda et al. 1995; Feigelson et al. 1995), Centaurus B (Tashiro et al. 1998), Abell85 0038-096 (Bagchi et al. 1998), 3C 295 (Brunetti et al. 2001), 3C 330 (Hardcastle et al. 2002), and 3C 263 (Crawford & Fabian 2003). Synchrotron self-Compton (SSC) emission was reported in the hotspots of several powerful galaxies, including Cygnus A (Harris et al. 1994), 3C 295 (Harris et al. 2000), 3C 273 (Röser et al. 2000), 3C 123 (Hardcastle et al. 2001), 3C 207 (Brunetti et al. 2002), and 3C 263 and 3C 330 (Hardcastle et al. 2002). Nonthermal X-rays of uncertain origin have recently been detected in the hotspots of 3C 280 and 3C 254 (Donahue et al. 2003).

When combined with radio observations, X-ray detections allow one to infer the mag-

netic field strength in an emitting region. Yet, in practice the derived fields vary significantly, depending on the assumed mechanism for X-ray emission. So, interpretation is often uncertain. Indeed, closeness to the equipartition value is sometimes used as a validation criterion for a magnetic field estimated by any other means. That seems unacceptable, since there is no convincing theoretical argument for equipartition between radio-emitting electrons and magnetic fields, and empirical evidence argues that not all sources are in equipartition (e.g., Centaurus B (Tashiro et al. 1998), PKS 0637-752 (Schwartz et al. 2000)).

There are obvious complications with all of the field measures. For example, deconvolution of the particle and field information also requires assumptions about the particle and field filling factors, as these values are impossible to extract from observations. For simplicity, a uniform magnetic field distributed through the emitting region is customarily assumed. As explained below, caution is needed, particularly when assuming magnetic field uniformity. It is important to be aware that the radio and X-ray emissions may be dominated by physically different regions in the source, and so one must be careful that the same particle population is sampled by the radio and X-ray observations. This paper is based on the expectation that synthetic observations of numerically simulated radio galaxies may help us understand these issues in a way that makes minimal use of convenient, simplifying mathematical assumptions, while retaining the benefit of complete knowledge of the actual physical conditions being observed.

Tregillis et al. (2001b) (Hereafter TJR01) recently carried out three dimensional time dependent MHD simulations of radio-jet flows that included nonthermal relativistic electron transport in space and momentum, enabling them to create the first synthetic radio observations from nonthermal electron distributions that were consistently evolved within the plasma flows. Those synthetic observations were used in conjunction with a detailed dynamical analysis to study how the dynamical and nonthermal particle transport processes lead to observable radio synchrotron surface brightness and spectral index patterns. Preliminary results of the synthetic observations were also reported in Tregillis et al. (2001a), Tregillis et al. (2002a), and Tregillis et al. (2002b).

Here we look anew at the simulation data presented in TJR01, shifting our attention from a dynamical analysis to the extraction of physical properties of the simulated objects using standard radio and X-ray observational analyses and then comparing results to the actual physical properties of the simulated objects. Through this effort we aim for new insights into how well standard analysis assumptions and techniques work to capture the true physical nature of a source. In addition, we attempt to identify crucial issues for successful extraction of physical properties of a given object. We emphasize that our purpose here is not to simulate specific real world radio galaxies. Neither do we intend to reevaluate the

observations and analyses of particular sources. Additional details and discussion can be found in Tregillis (2002).

The paper is structured as follows. § 2 provides a brief exposition of our numerical methods, a review of the model parameters from TJR01, and an overview of our synthetic observation techniques. These techniques are then applied to the models in §§ 3-5. In § 3 we look at what can be learned from the correlations between X-ray and radio surface brightness. § 4 is devoted to an examination of the magnetic field inferred from synchrotron and inverse-Compton surface brightness, B_{ic} and the minimum-energy field, B_{me} . Combined use of B_{ic} with the minimum-energy field B_{me} as a possible tool to estimate local nonthermal energy content is discussed in § 5. The key findings are then summarized in § 6.

2. METHODS

2.1. Numerics

Our numerical methods were detailed in Jones et al. (1999) and TJR01. In short, we follow the bulk flow through a 3D TVD Eulerian ideal MHD scheme and evolve a passive relativistic electron population on the Eulerian grid through the standard particle kinetic equation.

Our MHD code is based on an extension of the “Total Variation Diminishing” scheme (Harten 1983), as detailed in Ryu & Jones (1995) and Ryu et al. (1995). The code preserves $\nabla \cdot B = 0$ at each time step using a constrained transport scheme (Dai & Woodward 1998; Ryu et al. 1998). We include a passive “mass fraction” or “color tracer”, C_j , to distinguish material entering the grid through the jet orifice ($C_j = 1$) from ambient plasma ($C_j = 0$).

Our electron transport scheme takes practical advantage of the mismatch between bulk flow and diffusive transport scales for GeV electrons of relevance to radio and X-ray emissions within radio galaxies. In short, the lengths and times appropriate to the dynamics are orders of magnitude larger than those for electrons at energies relevant to radio synchrotron radiation. The electron momentum (energy) distribution, $f(p)$, is then sufficiently broad that it can be adequately represented by a piecewise power-law form within a few broad bins in momentum space. At shocks, rapid diffusive acceleration for $\lesssim 10$ GeV electrons ensures that they will emerge “instantaneously” from shocks with power-law momentum distributions. Subsequent, downstream cooling can be treated in a straightforward way. We therefore divide the momentum domain into a small number N of logarithmically spaced bins, and estimate particle fluxes across momentum bin boundaries by representing $f(p) \propto p^{-q(p)}$ within bins, where $q(p)$ varies in a regular way (Jones et al. 1999).

In the test-particle limit for diffusive shock acceleration used here, electrons emerge from shocks with a power-law spectral index $q = 3\sigma/(\sigma - 1)$, where σ is the shock compression ratio. The magnetic field is sufficiently weak in these simulations that all strong shocks behave dynamically essentially as hydrodynamic shocks. In accord with current understandings of collisionless shocks (e.g., Kang et al. (2002)) we also inject and accelerate electrons from the thermal plasma passing through shocks. Injection physics at shocks is still poorly understood, so we simply assume that a small fraction, ϵ , of the thermal electron flux through a shock becomes extended via diffusive shock acceleration into the aforementioned power-law beginning at momenta just above the postshock electron thermal values.

2.2. Simulated Jet Properties

Here we give a short rundown of the physical parameters of the three simulations first introduced and analyzed in TJR01. The models are summarized in Table 1, which is reproduced from TJR01.

The simulated MHD flows of TJR01 are dynamically identical. Each jet entered the grid with a simple “top hat” velocity profile with $M_j = u_j/c_a = 80$, where c_a is the sound speed in the uniform ambient medium. The jets entered the grid at $x = 0$ in gas pressure balance with the ambient medium and with a density contrast $\eta = \rho_j/\rho_a = 10^{-2}$, giving a jet-based Mach number $M_j = 8$. The initial jet core radius was $r_j = 15$ zones, while the entire $576 \times 192 \times 192$ uniformly zoned grid is $38\frac{2}{5}r_j \times 12\frac{2}{5}r_j \times 12\frac{2}{5}r_j$. In units of initial jet radius ($r_j = 1$) and ambient sound speed ($c_a = (\gamma P_a/\rho_a)^{1/2} = 1$, with $\gamma = 5/3$) the simulations stopped at $\tau_{end} = 5.4$ time units when the bow shock reached the boundary at $x = 38\frac{2}{5}$. In physical units, the jet radius $r_j = 2$ kpc and the inflow velocity $u_j = 0.05c$. This leads to a physical time unit $\approx 10^7$ years and a computational grid length ≈ 77 kpc. Open boundary conditions were used everywhere except at the jet orifice. The initial axial and background magnetic field ($B_x = B_{x0}$; $B_y = B_z = 0$) (also termed “fiducial” below) exerted a magnetic pressure 1% of the ambient gas pressure ($\beta = 10^2$). In addition to the axial component, B_{x0} , the in-flowing jet also carried a toroidal magnetic field component derived from a uniform axial current and a return current on the jet surface; i.e., $B_\phi = 2 \times B_{x0}(r/r_j)$ for $r \leq r_j$. To break cylindrical symmetry, we added a modest wobble to the in-flowing jet velocity; that is, it was slowly precessed on a cone of opening angle 5° with five periods during the run.

TJR01 presented three idealized examples of electron transport, designed to isolate individual transport behaviors. Those models are also summarized in Table 1. Here, briefly, are other vital details. Electrons were transported explicitly over the momentum range

$p_0 < p < p_N$ with $p_0 = 10$ and $p_N \approx 1.63 \times 10^5$ (with p in units of $m_e c$) for all models. Below p_0 the distribution function $f(p)$ was continued as a power-law. At p_N the gradient in the distribution function slope, $dq(p_N)/d \ln p$ was continued. Eight momentum bins ($N = 8$) were used for each simulation. Since the simulated nonthermal cosmic-ray electrons were passive, all results can be scaled for other choices of p_0 (p_N/p_0 is fixed). All three transport models included adiabatic cooling and diffusive shock acceleration, although second-order Fermi acceleration and Coulomb losses were neglected. In each model, the jet nonthermal electron population entered with a momentum index $q = 4.4$, representing a synchrotron spectral index, $\alpha = (q - 3)/2 = 0.7$, where $S_\nu \propto \nu^{-\alpha}$.

As listed in Table 1 we excluded local shock electron injection in Models **1** (hereafter called the “Control Model”) and **3** (hereafter called the “Cooling Model”), setting $\epsilon = 0$. Those models isolated evolutionary behaviors of pre-existing electron populations in the jet. In Model **2** the injection parameter $\epsilon = 10^{-4}$, so we label Model **2** the “Injection Model”. Details of these ϵ choices are given in Jones et al. (1999) and TJR01. We note that since the electron population in the simulation was passive, the Injection Model results could be simply rescaled for an alternate ϵ . The in-flowing jet nonthermal electron population in this model was made much smaller than the other two models, so that local enhancements of the electron populations at shocks could be isolated. The Control Model and the Injection Model are “adiabatic” in the sense that electrons experience negligible synchrotron aging. That feature eliminates convex spectral curvature, although some concave curvature can result from spatial mixing of dissimilar power-law populations. Model **3**, on the other hand, includes significant radiative aging from synchrotron and inverse-Compton processes, thus its Cooling Model label.

In order to parameterize radiative particle aging, we defined a characteristic synchrotron cooling time, τ_{s0} , for electrons with $p = 10^4$ in the fiducial magnetic field. For the adiabatic Models **1** and **2**, we set $\tau_{s0} = 1.6 \times 10^3$ (compared to $\tau_{end} = 5.4$) by setting $B_{x0} = 0.39 \mu\text{G}$ and ignored inverse-Compton losses, as well, to ensure negligible radiative aging for electrons of interest. For Model **3** we made $\tau_{s0} = \tau_{end} = 5.4$ by setting $B_{x0} = 5.7 \mu\text{G}$. Inverse-Compton losses from the CMB were taken into account by including a term with $B_{cmb} = 3.2 \mu\text{G}$ corresponding to the current epoch. Once again, the physical unit for τ in these simulations is approximately 10 Myr.

2.3. Synthetic Observation Techniques

Our synthetic observation technique is straightforward. We combine vector magnetic field and nonthermal electron distribution data from our simulations to calculate self-consistent

radio and nonthermal X-ray volume emissivities in every zone of the computational grid. In order to simplify the analysis we restrict emissions to zones dominated by bulk plasma originating at the jet orifice, by requiring $C_j \geq 0.99$. A raytracing procedure integrates along lines of sight in the optically thin limit to project emissions from the simulated objects on the sky for an arbitrary orientation. We write the output data in FITS format, and analyze it using conventional observational packages (MIRIAD and KARMA (Gooch 1995)).

Since the simulations are high resolution, the synthetic maps produced are of much higher resolution and dynamic range than typical real observations. To see the influence of resolution on our analysis we also have convolved the synthesized brightness distributions with circular Gaussian beams using the MIRIAD task CONVOL to several lower resolutions. For convenience, we placed all the objects at a fixed luminosity distance of 100 Mpc, although the choice has no influence on our conclusions. For this distance, the nominal unconvolved resolution is 0.28 arcseconds, and the projected jet length is about 110 arcseconds. We present results for convolved resolutions of 3.0 and 22.0 arcseconds as well, chosen to correspond to roughly 37 and 5 telescope beams along the jet, respectively. These choices, while arbitrary, match qualitatively what is commonly achieved in many real source observations. All synthetic observation images are set to 512×512 pixels (not every pixel contains a nonzero brightness value, however).

As in TJR01 we confine our discussion to one representative point in time; namely, $t = 4.0$ in simulation units or about 4×10^7 yr. All synthetic observations in this chapter refer to the same source orientation on the sky as that used in TJR01, in which the jet axis is about 45 degrees from the plane of the sky. Our conclusions are unaffected by these choices. The bulk flow is nonrelativistic, so no Doppler corrections have been applied.

2.3.1. Radio Synchrotron Emissivity

In each spatial zone we compute a synchrotron emissivity based on the local vector magnetic field, \mathbf{B} , and nonthermal electron distribution, $f(p)$, as evolved by our transport scheme. As given by Jones et al. (1974), the emissivity is

$$j_s(\nu) = j_{\alpha 0} \frac{4\pi e^2}{c} f(p_s) p_s^q \left(\frac{\nu_{B\perp}}{\nu} \right)^\alpha \nu_{B\perp}. \quad (1)$$

The spectral index α is related to the local electron momentum index q via $\alpha = (q - 3)/2$, $\nu_{B\perp} = eB \sin \Omega / (2\pi m_e c)$, where Ω projects the local field onto the sky, and $j_{\alpha 0}$ is an order-unity dimensionless constant, defined in Jones et al. (1974). For a selected observing frequency, ν , the distribution, $f(p_s)$, and the index, q , are determined for each point on the grid by establishing the relevant electron momentum from the relation $p_s = [2\nu / (3\nu_{B\perp})]^{(1/2)}$,

with p_s in units $m_e c$. We note for the magnetic fields in our simulated objects and radio frequencies in the GHz band that typical $p_s \sim 10^4 - 10^5$.

2.3.2. X-ray Emissivities

We compute an X-ray emissivity, j_X , including inverse-Compton contributions from the CMB (Hereafter IC/3K) and synchrotron self-Compton (SSC); viz, $j_X = j_{3K} + j_{SSC}$. We ignore inverse-Compton scattered AGN photons, as well as X-ray synchrotron emission. Although we include SSC emission, since its analysis does provide some useful insights, we mention that it is typically several orders of magnitude less intense in our simulated objects than IC/3K emission.

The X-ray IC/3K emissivity, $j_{3K}(\nu_X)$, can be simply expressed at a selected X-ray frequency, ν_X , in terms of the synchrotron emissivity, $j_s(\nu_X)$, in equation (1) extrapolated to ν_X ; namely Jones et al. (1974),

$$j_{3K}(\nu_X) = e_{\alpha 0}^{3K} \frac{\sigma_{TC}}{e^2} \frac{cu_\mu \nu_\mu^{\alpha-1}}{4\pi \nu_{B\perp}^{1+\alpha}} (1+z)^{3+\alpha} j_s(\nu_X), \quad (2)$$

where $u_\mu = aT_0^4$ and $\nu_\mu = kT_0/h$ are the energy density and characteristic frequency, respectively, at the current epoch of the CMB, while $e_{\alpha 0}^{3K}$ is another order-unit constant that can be obtained from Jones et al. (1974). We note in equation (2) that $j_s(\nu_X)$ is normalized and α is determined at $p_\mu = (\nu_X/\nu_\mu)^{1/2}$. For $h\nu_X = 1.2 - 7.5\text{keV}$, considered below, $p_\mu \approx 2 \times 10^3 - 5 \times 10^3$, which is substantially less than momenta responsible for the GHz synchrotron emission.

The SSC emissivity, j_{SSC} , depends upon the synchrotron intensity distribution incident upon each zone. To keep the calculation manageable, we adopt the common approximation of an isotropic incident intensity, so that j_{SSC} can be expressed in terms of the omnidirectional incident flux, Φ_ν^S . Except when the radiation field is dominated by a very intense anisotropic local source, this approximation should be good, so adequate for our present purposes. Then, using a convenient expression in terms of the IC/3K X-ray emissivity from the same electron population we have (Jones et al. 1974),

$$j_{SSC}(\nu_X) = e_{\alpha 0}^{SSC-3K} \left(\frac{\Phi_{\nu_k}^S \nu_k^{\alpha_k}}{cu_\mu \nu_\mu^{\alpha-1}} \right) \ln \left[\frac{2}{3} p_N^4 \frac{\nu_{B\perp}}{\nu_X} \right] j_{3K}(\nu_X). \quad (3)$$

Here α_k is the synchrotron spectral index at the low-frequency synchrotron cutoff ν_k , and α is the spectral index determined for equation (2). The constant $e_{\alpha 0}^{SSC-3K}$ is order-unity and obtainable from Jones et al. (1974). We note that since the dominant synchrotron

emission occurs at much lower frequencies than ν_μ , electrons responsible for SSC emission are generally of higher energy than those producing the IC/3K emission.

We use a simple and fast FFT-based scheme to estimate the omnidirectional synchrotron flux Φ_ν^S . Details of the calculation can be found in Appendix A.

3. RESULTS: RADIO AND X-RAY BRIGHTNESS CORRELATIONS

We begin with a brief, qualitative comparison between the synthetic radio and X-ray brightness distributions. Radio surface brightness maps for the three models were shown in TJR01. Here, Figures 1 through 3 show the corresponding IC/3K and SSC X-ray surface brightness images. From the images it is apparent that dominant dynamical features such as the jet and the radio hotspots are visible in both bands, but also that many details differ. For instance, X-ray brightness distributions are smoother, with much less dynamic range than the radio distributions. This simply reflects the fact that the inverse-Compton brightness represents only the column density of relativistic electrons over a narrow range of electron energies. The synchrotron brightness also depends strongly on the (intermittent) magnetic field distribution.

In §§4 and 5 we will combine the synthetic radio and X-ray data to explore their effectiveness for inferring source magnetic field properties. First, however, we demonstrate that some basic dynamical relationships connecting particles and fields can be extracted from correlations between the various intensity distributions, which are shown in Figures 4, 5 and 6. As we examine our three simulated objects, we should keep in mind that the magnetic field structures are identical in all three models, except for magnitude; only the nonthermal electron distributions differ. Also, we emphasize, once again, that our goal is to examine ways of extracting reliable information about the objects we have in hand; that is, how we extract from observations the physical properties that are actually present. Because we know their properties exactly, the simulated objects are uniquely valuable testing grounds, independent of how closely those detailed properties match astrophysical objects.

Figures 4 and 5 are scatter plots of 7.5 keV IC/3K and SSC intensities versus 2.9 GHz radio intensity, respectively, for the three electron transport models (Table 1). Similar distributions would be obtained for other observing frequency choices. Every other nonzero pixel is represented, for just under 2.5×10^4 points in each plot. In each panel the X-ray and radio brightness distributions are broadly correlated. It is possible to extract from these trends insights about the dynamical behaviors of the source magnetic fields, as we illustrate. We emphasize, however, that at a given radio (X-ray) brightness, the X-ray (radio) intensities

generally spread over more than an order of magnitude, so it would be unrealistic to try to predict the inverse-Compton brightness distribution from the radio distribution or vice versa. This is especially so in the lobe structure, where the spread in synchrotron brightness is enormous, due to the wide range of magnetic field strengths.

Comparison between Figures 5 and 4 shows that the SSC brightness distributions of our simulated objects are generally several orders of magnitude less than the IC/3K intensities. The difference is more than 10 orders of magnitude for both the Control Model and Injection Model, where the magnetic field magnitude was set very small to reduce synchrotron energy losses. Even for the Cooling Model, with its stronger field, the SSC intensities are mostly three to four orders of magnitude less than the IC/3K intensities. This behavior comes from the fact that the synchrotron omnidirectional flux is generally much smaller than the CMB omnidirectional flux in our simulated objects. That mirrors the situation in real radio galaxies, as well, since only the most intense X-ray hotspots have been found to be SSC dominated (e.g., Harris et al. 2000). Despite this, it is instructive to include the SSC brightness distributions in our analysis, since they reveal some useful insights.

The IC/3K vs radio trends in Figure 4 are well described for all three models by the proportionality $I_{IC/3K} \propto I_S^m$, with $m \approx 1/3 - 1/2$. To understand this, suppose the local magnetic field scales with the electron density as $B \propto n_e^b$. Since $I_{IC/3K} \propto n_e \mathcal{D}$ and $I_S \propto n_e \mathcal{D} B^{1+\alpha}$, where \mathcal{D} is the path length, we have $I_{IC/3K} \propto I_S^{1/(1+b(1+\alpha))} \equiv I_S^m$.

On the other hand, by standard arguments $B \propto \rho^{2/3}$ for a disordered field in compression-dominated flows. Assuming $n_e \propto \rho$, this gives $m = 3/(5 + 2\alpha)$. For $\alpha \sim 0.5 - 1$, typical of the synthetic radio sources, this would give $m \sim 0.5 - 0.43$. Alternatively, at perpendicular shocks one expects $B \propto \rho$, resulting in $m = 1/(2 + \alpha)$, or $m \sim 0.4 - 0.33$. Thus, the observed trends are consistent with field evolution dominated by these dynamical processes. On the other hand, field evolution controlled by stretching of flux tubes would satisfy $B \propto \ell$, where ℓ is the length of the flux tube (e.g., Gregori et al. 2000). There is no explicit interdependence between density and magnetic field. We know that the magnetic fields in the simulated object are filamented, so flux tube stretching certainly takes place. The above exercise brings out the fact that the global field evolution in the simulated object is dominated by compression, however. This matches our conclusions about the simulated field behaviors in TJR01. Sheared field evolution, while clearly involved and locally important, predominantly adds scatter to the correlations in Figure 4.

With the notable exception of the dominant hotspot in the Injection Model, the SSC and radio intensity distributions follow similar correlations as the IC/3K-radio correlation; namely, $I_{SSC} \propto I_S^m$, with $m \approx 1/3 - 1/2$. From this match between SSC and IC/3K trends one might expect that $I_{SSC} \propto I_{IC/3K}$, and this is nicely confirmed for the Control

Model in Figure 6. This proportionality is also evident in the other two models, excepting the Injection Model hotspot, although there is a lot more scatter.

For the general distribution we note from equation 3 that one can write $I_{SSC} \propto \Phi^S I_{IC/3K}$. The observed correlations then imply, especially for the Control Model, that $\Phi^S \approx \text{constant}$ within the radio lobes. That represents the fact that the average omnidirectional flux for the source is a good approximation to the local flux at any point in the source. This follows if the omnidirectional synchrotron flux at each point is dominated by the collective contributions of distant emissions within the source. In that case the average synchrotron emissivity becomes an effective value to use in estimating the SSC emission from the object.

The situation is much different in the dominant Injection Model hotspot. The SSC/radio intensity correlation is described by $m \sim 1 - 1.5$, whereas the SSC and IC/3K intensities follow $I_{SSC} \propto I_{IC/3K}^{2.5-3}$. On the other hand, the correlation between IC/3K and radio surface brightness is similar to what is seen elsewhere in the source and in the other two models. Previously, we interpreted the IC/3K vs radio correlation as evidence for magnetic fields evolving according to the scaling $B \propto n_e^{2/3}$, which, therefore, seems applicable in the hotspot, as well. It is the SSC behavior that is different in the Injection Model hotspot, and the distinctive correlations there can be understood by supposing that $\Phi^S \propto I_S$; that is, the synchrotron radiation field is dominated by local emissions in the hotspot, as we might expect. Using again the emissivity relations in §2.3 we can write in this case that $I_{SSC} \propto I_S^{(8+2\alpha)/(5+2\alpha)}$ and $I_{SSC} \propto I_{IC/3K}^{(8+2\alpha)/3}$. Taking $\alpha \approx 0.65$ for the Injection Model hotspot radio spectral index we would predict $I_{SSC} \propto I_S^{1.47}$ and $I_{SSC} \propto I_{IC/3K}^{3.1}$, very close to what is observed.

Finally, we note that on the whole SSC X-ray emission is no more tightly correlated with the radio intensity than is the IC/3K intensity, despite the fact that it is a consequence of the radio emission itself. That comes from the fact that the SSC emissivity reflects radio emissions throughout the source, not just the local radio emission. Small regions of high radio brightness embedded in more diffuse emission tend to wash out the SSC/radio correlation, because they act like internal point sources that anisotropically illuminate their neighborhoods. If the surrounding emission is particularly diffuse, such regions may contribute flux at considerable distances throughout the source. That effect is particularly striking in the Injection Model, where the very bright radio hotspot is compact and surrounded by more diffuse radio emission.

4. RESULTS: ESTIMATED MAGNETIC FIELD STRENGTHS FROM OBSERVED INTENSITIES

As mentioned in the introduction, total synchrotron intensities are commonly applied in two ways to estimate magnetic field strengths in optically thin synchrotron sources. This is not straightforward, of course, since synchrotron intensity from an optically thin source alone cannot determine the strength of the source magnetic field. Some additional information must be supplied. The more traditional and still most-common method minimizes the total energy (or sometimes pressure) for the relativistic particles and magnetic field, or what is close to the same thing, an equipartition is assumed between them. A second, and increasingly common method combines information carried in the synchrotron intensity with observed inverse-Compton scattered intensities presumably produced by the same electron population. There are serious uncertainties in the application of both methods, ranging from the absence of convincing theoretical arguments for the minimum energy condition in an unrelaxed system to the likelihood of inhomogeneous magnetic field and particle distributions. In this section we will apply standard methods for these two approaches to synthetic observations of our simulated objects in order to see how they compare and to understand better how the inferred field properties match actual conditions for objects with complex, quasi-realistic structures.

4.1. The Analysis Procedure

For this exercise we “observed” synchrotron emission at $\nu = 2.9$ GHz and IC/3K emission at 1.2 keV in all three models. To explore the connections between observationally inferred magnetic fields and actual magnetic field distributions we selected six lines of sight (LOS) for close analysis. Those LOS are marked in Figure 7. Two of the LOS pass through lobe structures (**LOS 1**, **LOS 4**). Three penetrate the jet (**LOS 3**, **LOS 5**, **LOS 6**) and one centers on the dominant hotspot (**LOS 2**). **LOS 4** allows us to look at the influence of particle aging on the analyses, since the spectrum there is strongly convex in the Cooling Model. Similarly, **LOS 5** shows a concave spectrum in the Injection Model, due to strong blending of dissimilar power-law electron distributions introduced at shocks. (These spectra along **LOS 4** and **LOS 5** are shown in Figure 8.) **LOS 6** passes through the jet base, where magnetic field and particle populations are particularly simple, and known from the jet inflow conditions.

Magnetic field strength can be calculated very simply from synchrotron and IC/3K intensities for a uniform medium when the electron distribution is a power-law. We used the following expression for this estimated field, B_{ic} (e.g., Jones et al. 1974; Harris & Romanishin

1974; Harris & Grindlay 1979):

$$B_{ic}^{1+\alpha} = (1.06 \times 10^{-11}) (2.09 \times 10^4)^{\alpha-1} (1+z)^{3+\alpha} \times \left(\frac{\nu_r}{\nu_X} \right)^\alpha \left(\frac{j_{\alpha 0}^{3K}}{j_{\alpha 0}} \right) \frac{I_S(\nu_r)}{I_{IC/3K}(\nu_X)} \mu\text{Gauss}. \quad (4)$$

For uniform particle and field distributions, this expression is exactly equivalent to inverting the analytic calculation of synchrotron and IC/3K surface brightnesses in our synthetic observations.

Similarly, the standard expression used to compute the minimum-energy magnetic field, B_{me} , is (Miley (1980))

$$B_{me} = 5.69 \times 10^{-5} \left[\left(\frac{1+k}{\eta} \right) \frac{F(\nu_r)}{\nu_r^{-\alpha}} \frac{(1+z)^{3+\alpha}}{\theta_x \theta_y \ell \sin^{3/2} \vartheta} \right]^{2/7} \times \left[\frac{\nu_2^{1/2-\alpha} - \nu_1^{1/2-\alpha}}{(1/2-\alpha)} \right]^{2/7} \text{ Gauss}. \quad (5)$$

Here $F(\nu_r)$ is the observed radio flux density within an observing beam, $k \equiv U_{proton}/U_E$, η is a magnetic field volume filling factor, ϑ is the angle between the magnetic field and the line of sight, θ_x and θ_y are the semimajor and semiminor axes of the observing beam in arcseconds, ℓ is the path length through the source in kpc, and ν_1 and ν_2 are the *fixed* lower and upper synchrotron cutoff frequencies in the source frame, expressed in GHz. Note that while B_{me} is expressed in terms of synchrotron flux density, it really depends on the mean $I_S(\nu_r)/\ell$; that is, the mean synchrotron emissivity. We assume below for simplicity that $k = \eta = \sin \vartheta = 1$. The magnetic field is so tangled and intermittent that assuming $\sin \vartheta = 1$ introduces errors of only a few percent into our analysis.

In order to incorporate the full nonthermal electron distributions as well as possible into B_{me} , the frequency limits needed in equation (5) correspond in each model to the characteristic synchrotron frequencies of the lowest and highest energy electrons and the fiducial magnetic field for each model (see Table 1). Those turn out to be $\nu_1 = 100$ Hz and $\nu_2 = 30$ GHz for the Control Model and the Injection Model; for the Cooling Model $\nu_1 = 1500$ Hz and $\nu_2 = 450$ GHz. Our conclusions do not depend on any of these parameter choices.

We note that since both empirical field measures depend only on intensities, they are independent of distance assumptions. Nevertheless, for consistency with our discussions in TJR01 we place the objects at a distance of 100 Mpc, giving 0.28 arcseconds for the projected size of a numerical resolution element.

Summaries of our analysis are given in Table 2 and Figure 9. At high resolution, B_{ic} generally falls within a factor of two of B_{rms} in the sampled volume. B_{me} , on the other hand, can show considerably larger scatter, over an order of magnitude in some cases, depending on the specifics of the particle transport. Both estimates are sensitive to spectral curvature. Estimates for jet structures tend to show less scatter than for lobe structures, which typically embody a wider range of physical conditions. Results for 3.0 and 22.0 arcsecond Gaussian beams are also included in Table 2. The influences of bigger beams are predictable in that derived fields resemble the analogous properties of the larger regions surveyed.

Figure 9 compares B_{ic} and B_{me} to B_{rms} . It is evident that both empirical magnetic field estimates correlate roughly with B_{rms} along the selected lines of sight. The bolometric synchrotron intensity does depend on the rms magnetic field along the line of sight, of course. The spectral emissivity $j_s(\nu) \propto B^{1+\alpha}$, is similar, since in our sources $\alpha \sim 0.7 - 1$ are common. Still it is not obvious a priori how well such a simple measure as B_{rms} should compare to inferred values, so the experiment is valuable. Two-thirds of the B_{ic} (B_{me}) points are within a factor of two (three) of B_{rms} . On the other hand, while the B_{ic} values are approximately randomly distributed with respect to B_{rms} , there are obvious biases in B_{me} that are dependent on the electron transport model in the simulation. Those biases correctly reflect actual deviations from the minimum energy condition. In particular, our simulated objects are not in electron/magnetic field energy equipartition. Nor, as we will discuss in §5, is there physics in the simulations expected to produce this kind of equipartition.

Magnetic field profiles for each of the LOS are shown in Figure 10 for the Control Model and Injection Model. The field distributions in the Cooling Model are identical to the other two sources except for being everywhere a factor 14.8 times larger. However, since the particle populations evolve differently in the Cooling Model, the inferred magnetic field behaviors are not necessarily the same as in either of the other two models. Points where $C_j < 0.99$ are set to zero in this analysis; that is, we filtered out plasma that did not originate in the jet in order to match the assumptions made in computing nonthermal emissions. In this regard we comment that the contact discontinuity between the “jet plasma” and the “ambient plasma”; i.e., the boundary between $C_j = 1$ and $C_j = 0$, is not simple. It is actually quite convoluted, so that distinct fingers of ambient plasma penetrate into the cocoon. Consequently, there are “dropouts” in the emission and associated physical variables according to the prescription we have followed; that is, these regions do not contribute to B_{ic} , B_{me} , nor to B_{peak} or B_{rms} .

In §5 we will explore how effectively B_{ic} and B_{me} can be used to reveal information about the partitioning of energy between magnetic fields and nonthermal electrons. Here we focus on the two field estimators separately. We summarize the important features in the

next subsection.

4.2. Field Properties on Selected Lines of Sight

In this section we look directly at the properties of the magnetic field along the individual selected LOS as revealed in Figure 10.

LOS 1 and **LOS 4** pass through the diffuse lobe of the sources. Both lines exhibit very complex magnetic fields, and considerable entrainment of ambient plasma into the lobe structure is evident from the large number of “dropouts” in Figure 10. The strongest field regions are revealed as the relatively bright filaments in Figures 1-3 and Figure 7 (see also Fig. 5 in TJR01). The nonthermal electron density also exhibits much fine structure (not shown), as one would expect from the discussion in §3. While the IC/3K-radio analysis (§3) indicates the field and particle structures are correlated, it also shows very wide scatter, especially in the lobes, where flows are chaotic. That does impact on B_{ic} as a quantitative field measure.

Except for one case (**LOS 4** in the Cooling Model) values of B_{ic} along these lobe LOS all fall below B_{rms} . This bias results from the presence of substantial electron populations in weak field regions that contribute little to the radio emission, but that do produce X-rays. In effect the IC/3K intensity provides an overestimate of the number of radio emitting electrons, so that under the uniform source hypothesis the field apparently needed to account for the radio emissions is weakened. On the other hand, a comparison with Figure 10 shows that B_{ic} for the Control Model and Injection Model are representative of the field values being sampled along both LOS, so it does give a “meaningful” result, if not a simply defined quantitative one.

The relatively higher value of B_{ic} for the Cooling Model on **LOS 4** is a consequence of spectral aging; that is, the spectrum is convex. Intentionally, no correction was made for this effect, in order to expose its potential influence. Recall that the 1.2 keV IC/3K emission used to compute B_{ic} comes from 1 GeV electrons, while the 2.9 GHz emission is produced by electrons with energies about an order of magnitude higher, even in the strongest field regions along this LOS. With a convex electron spectrum the computed B_{ic} will be artificially increased, as simple arguments can show. Suppose, for example, we measured the bolometric synchrotron intensity, I_S , from electrons of energy γ_S and the bolometric IC/3K intensity, I_{3K} , from electrons of energy γ_{3K} . If the object were homogeneous, and we fixed the observed radio band, it is simple to show that $B \propto (I_S/I_{3K})N_{\gamma_{3K}}/N_{\gamma_S}$, where $N_{\gamma_{3K}}$ and N_{γ_S} represent the number of electrons required to produce the observed intensities. If we assumed that

$N_{\gamma_{3K}}$ and N_{γ_S} were connected by a powerlaw in γ with the powerlaw index determined by the high energy electrons responsible for the radio band, but the distribution is actually convex, we would always overestimate B , since we would overestimate $N_{\gamma_{3K}}/N_{\gamma_S}$. This same influence has an even more striking impact on the value of B_{me} for the Cooling Model on **LOS 4**. Under the equipartition that accompanies the minimum energy assumption, the effective overestimate of the electron population also exaggerates the estimated magnetic field energy, leading to an estimated magnetic field about two orders of magnitude greater than B_{rms} and an order of magnitude greater than B_{peak} along this LOS. Thus, it is very important when analyzing sources that exhibit “aged” spectra to account for the curvature when calculating the electron energy (I. L. Tregillis and L. Biggs, in preparation).

The values of B_{me} found in the Injection Model along these LOS, by contrast are almost an order of magnitude below the RMS field values. This correctly reflects the fact that the magnetic field energy in this model actually does greatly exceed the nonthermal electron energy in most locations that generate synchrotron emission.

LOS 3, **LOS 5** and **LOS 6** intersect the jet. B_{ic} values are close to B_{rms} in each model when the highest resolution is used in the observations. For the Control Model and Cooling Model the inferred field is almost independent of angular resolution. The Injection Model jet is relatively less dominant in accounting for emissions, since the radiating electron population is small there. At high resolution the inferred field is also close to B_{rms} . The concave property of the synchrotron spectrum on **LOS 5** in the Injection Model has at most a modest depressing influence on B_{ic} . As beam size increases on **LOS 3** and **LOS 5**, B_{ic} in the Injection Model increases markedly, because emissions become influenced by the nearby hotspot, where the electron population increases dramatically. That influence is greater in the Injection Model since its hotspot is much more intense than in the other two models (see Fig. 4).

B_{me} values follow a similar pattern to those seen in B_{ic} for lobe LOS; that is, the relation between B_{me} and B_{rms} follows the actual relationship between nonthermal particle and magnetic field energies in the predominant emission regions.

LOS 6 passes through the jet near its origin. In Figure 10 the jet is contained roughly between position coordinates 245 - 295, measured in computation zones. The magnetic field structure is simple and approximates that introduced at the computational boundary. Indeed, for all three models B_{ic} is very close to B_{rms} as well as the projected axial base jet magnetic field in the simulation.

LOS 2 passes through a hotspot resulting from a shock produced as the jet impinges on the near boundary of its cocoon. The magnetic field is relatively compressed and organized

there, accounting for the dominant peak in the field distribution near line coordinate 200. Virtually all of the radio emission in this direction originates in the hotspot, so that the B_{ic} and B_{me} values for all three models lie close to B_{rms} , irrespective of angular resolution. This is the only LOS we sampled that returns a B_{me} estimate in the Injection Model that is close to B_{rms} . It is, in fact, the only LOS we sampled that has emissions in that electron transport model predominantly from regions close to electron/magnetic field equipartition.

5. RESULTS: OBSERVATIONAL ESTIMATION OF PARTICLE/FIELD ENERGY PARTITIONING

In the previous section we found that a synchrotron/inverse-Compton analysis provides reasonable estimates of characteristic magnetic fields, in particular B_{rms} , in our simulated objects. There are biases that can degrade the estimates when the fields are significantly more intermittent than the nonthermal electrons or when the electron energy spectra are strongly aged. However, the B_{ic} values we derived were mostly within a factor of two of the RMS fields. On the other hand the minimum energy magnetic fields were close to the RMS fields (or any other simple statistical measure) only when the emission was dominated by relativistic plasma close to equipartition. That is what we should hope for and expect, of course. At the same time, we noted that the biases in B_{me} correctly reflected the degree of deviation from equipartition of the dominant plasma.

This suggests that combining B_{ic} and B_{me} might reveal a meaningful estimate of the ratio of nonthermal electron and magnetic field energy and, consequently, provide an improved estimate of the total nonthermal energy compared to the minimum energy. We test that possibility in this section for our simulated objects, where we not only can perform radio and X-ray observations, but also know the internal energetics directly.

5.1. The Analysis Procedure

The obvious parameter for comparing magnetic and nonthermal particle energies is the ratio of their local densities; namely,

$$d \equiv \frac{U_B}{U_E}. \quad (6)$$

Standard expressions for the minimum-energy magnetic field, B_{me} , (i.e., assuming a uniform source and a power-law $f(p)$, and a fixed frequency band) (see eq. [5]), lead to the

simple relation

$$d = \frac{3}{4}(1+k) \left(\frac{B}{B_{me}} \right)^{7/2}, \quad (7)$$

where B is the actual field strength. The exact value of k makes no substantial difference to our conclusions, so for convenience we will still apply the commonly used value $k = 1$. The total energy density in nonthermal particles and magnetic fields, U_T , is then obviously

$$\begin{aligned} U_T &= U_B \left(1 + \frac{1+k}{d} \right) \\ &= \frac{3}{7} U_{me} \left[\left(\frac{B}{B_{me}} \right)^2 + \frac{4}{3} \left(\frac{B_{me}}{B} \right)^2 \right], \end{aligned} \quad (8)$$

where $U_{me} = (7/3)(B_{me}^2/(8\pi))$ is the combined minimum energy density.

It is convenient to define $d_{min} \equiv \frac{3}{4}(1+k)$ corresponding to $B = B_{me}$. For $k = 1$ this gives $d_{min} = 1.5$. Using d_{min} we can write simply

$$d = d_{min} \left(\frac{B}{B_{me}} \right)^{7/2}, \quad (9)$$

or

$$\frac{B}{B_{me}} = \left(\frac{d}{d_{min}} \right)^{2/7}. \quad (10)$$

Note for the discussion below, when $d \gg 1$ ($d \ll 1$), that $U_T \propto d^{4/7} U_{me}$ ($U_T \propto d^{-4/7} U_{me}$).

To set the stage for our discussion we note that the jet inflow boundary conditions discussed in §2.2 give $d_0 = 0.16$ for the Control Model and the Cooling Model. Thus, these two jets enter the grid relatively close to electron/field equipartition. Accordingly, from equation (10) one finds at the jet orifice that $B \approx 0.5 B_{me}$. In contrast, the Injection Model jet enters very far from equipartition, with $d_0 = 1.6 \times 10^3$, so $B \approx 7.3 B_{me}$.

How should we expect d to change from these input values as the flows evolve? Recall that in our simulations particle energies are dominated by the thermal population; the nonthermal electrons are “test particles” that respond to the underlying flow dynamics, which is based on otherwise fully consistent MHD. The expected variation of d under adiabatic compression in those flows is straightforward to estimate. Recall from §3 that compression of an isotropic magnetic field varies $B \propto \rho^{2/3}$, so that $U_B \propto \rho^{4/3}$. We found in §3 that this behavior seems to account for much of the field structure in the lobe. At the same time, the nonthermal electron gas is relativistic, so $U_E \propto \rho^{4/3}$, as well. Thus, we may expect adiabatic expansion or compression to produce relatively little change in d .

On the other hand, in sheared flows B may have little or no correlation with ρ . In particular, an incompressible stretched flux tube has a field strength depending only on the length of the tube (see §3), which could produce very large increases in d inside flux tubes.

Variations of d across shocks are also difficult to quantify, although qualitatively we can expect d to decrease there, perhaps by a large factor. At most $U_B \propto \rho^2$ (in a perpendicular shock), but U_E should increase more strongly than this in response to diffusive shock acceleration. As shock strength increases the jump in U_B increases asymptotically, but the jump in U_E does not, both due to the diffusive reacceleration of the incident particle flux and also to any fresh injection due to “thermal leakage” at the shock.

5.2. Comparison Between Inferred and Actual Energetics

Because of initial conditions, most regions within the Control Model and Cooling Model *coincidentally* lie within an order of magnitude of this equipartition condition, with nonthermal electron energy being typically somewhat greater than magnetic field energy (see Figs. 12,14). In contrast for much of the source volume in the Injection Model, magnetic field energy greatly exceeds the nonthermal electron energy density (Fig. 13). That contrasting condition simply reflects the small population of nonthermal electrons entering with the jet in this model. It conveniently provides an excellent opportunity to study how different energy balances between particles and fields reveal themselves through their emission properties.

We again use the selected **LOS 1 - 6** to explore how energy partitioning inferred from observations compares to actual physical conditions within the sources. Table 3 lists the RMS and mean values, d_{rms} and $\langle d \rangle$, along each line of sight, as well as the value of d_{obs} inferred from the ratio B_{ic}/B_{me} used in equation (9), with $k = \eta = \sin \vartheta = 1$. The direct values of d were computed from the magnetic field strength in each numerical bin and the nonthermal electron energy density integrated between $p_0 = 10$ and $p_N = 1.63 \times 10^5$, corresponding to the synchrotron cutoffs assumed in calculating B_{me} . Figure 11 shows graphically the relationship between the d_{obs} and $\langle d \rangle$ data in Table 3. For comparison, Figures 12-14 display distributions of d along **LOS 1-6** using the actual, full nonthermal electron distribution and the magnetic field properties from the simulations. Average values, $\langle d \rangle$, are indicated in those plots by the dotted lines and d_{obs} by dashed lines.

First looking at Figure 11 we see a rough correspondence between d_{obs} and $\langle d \rangle$ for most of the data. On the other hand agreement is not generally better than about an order of magnitude. From equation (8) that would correspond to an uncertainty in the total energy of about a factor of four, if U_{me} were known precisely. We should not expect exact

correspondence, since d_{obs} is based on two indirect measures weighted to different points along each line of sight. We note below a couple of evident patterns that are useful to examine in order to obtain better insights to the limits of information contained in d_{obs} .

The two lobe LOS (**LOS 1** and **4**) in the Cooling Model give d_{obs} values two and four orders of magnitude, respectively, below $\langle d \rangle$. This strong bias is once again due to the influence of spectral aging in the lobes of this model, which have not been corrected for in this simple experiment. That is, if the electron spectrum is convex, one must be careful to count properly the low energy electrons, or B_{me} will be seriously over estimated, which has an even larger impact on d_{obs} . Most of the other LOS in the Control Model and the Cooling Model scatter reasonably around the $d_{obs} = \langle d \rangle$ line within about a factor of 4, and examination of Figures 12 and 14 shows that d_{obs} is usually “representative”. In that regard it is worth noting along the jet **LOS 3, 5** and **6** that d_{obs} agrees well with physical values of d in the jet itself, which is the dominant emission source. On the other hand d_{obs} for the Control Model hotspot (**LOS 2**) misses the actual energy partitioning in the hotspot by about a factor of seven. Here the field geometry is more complex, so that B_{me} is an under estimate of B in the hotspot, even though it exceeds B_{rms} along the LOS.

All of the d_{obs} values in the Injection Model fall significantly below $\langle d \rangle$. The closest match comes from **LOS 6**, which is dominated by the (simple) jet base. Otherwise, in this model there are very large fluctuations in d that do not correspond well to the strongest emission regions. So, in this model $\langle d \rangle$ is biased upwards compared to values representative of the emitting plasma and that determine d_{obs} .

The estimation of the local energy partitioning d based on B_{ic} and B_{me} works best in regions that are not strongly influenced by radiative aging and where the partitioning is not expected to vary strongly over short distances, such as inside jet structures. There is increasing evidence that the X-ray emission observed from some jets is doppler-boosted IC/3K emission (e.g., Tavecchio et al. 2000; Sambruna et al. 2001; Celotti et al. 2001). In that case this kind of analysis could be useful still, but it would require taking beaming and boosting effects into account, which we have not done because the flows here are nonrelativistic. That obviously adds another level of uncertainty, since those corrections can be large. Our analysis here was directed at the simpler case, but one that still contains many real world features that must be accepted in any complex synchrotron source.

6. CONCLUSIONS

We have performed extensive synthetic radio and X-ray observational analyses of the numerically simulated radio galaxies introduced in TJR01. These are the first synthetic observations with sufficient detail to allow the application of standard observational techniques to numerical simulations of radio galaxies. Standard observational techniques were applied to the simulation data in order to understand better how these techniques recover physical properties of observed objects. The simulated objects have the advantage of known physical properties and evolve with many fewer simplifying assumptions than required in analytic studies of this kind. We emphasize that our goal was to compare observed properties with known physical properties, not to present the simulated objects as direct models for real objects. Our models were intentionally idealized to isolate important nonthermal particle transport behaviors. We concentrated in this paper on magnetic field strength and source energy content calculations derived from synchrotron and inverse-Compton intensities. An analysis of information extracted through polarimetry will be presented in a forthcoming companion paper.

We enumerate some of the practical messages from our analysis:

1. The synchrotron to inverse-Compton intensity ratio provides a reasonable tool for estimating magnetic field strengths in complex radio sources when the inverse-Compton photons come predominantly from the CMB. In our synthetically-observed simulated radio galaxies the standard radio/X-ray analysis returned magnetic field values that fell within about a factor two of the RMS field in a sampled volume, unless the electron spectrum was strongly convex; i.e., in the absence of strong aging. Strongly aged spectra return field values that are too high, so need to be corrected for that effect. The effectiveness of this tool seems to apply even in regions where the electron distribution and the field structure are spatially intermittent; i.e., where they have small filling factors, such as in the lobes of the simulated radio galaxies. It is largely independent of the relative partitioning of energy between electrons and magnetic field.
2. The standard synchrotron emission minimum energy analysis returns magnetic field values consistent with the RMS fields only when the actual energy partitioning between electrons and fields is close to equipartition. Otherwise the inferred fields are biased in directions that correctly reflect the actual deviations from equipartition in the regions being sampled. In addition, our analysis demonstrated that minimum energy estimates based on strongly aged spectra can seriously overestimate the actual minimum energy magnetic field, unless the spectral curvature is properly accounted for.
3. The energy partitioning and the total source energy can be roughly estimated utilizing

the ratio of the minimum energy magnetic field to that inferred from the relative synchrotron and inverse-Compton intensities. In our analysis the actual energy content was recovered to within a little better than an order of magnitude, once again in the absence of strong spectral aging. Without correction, however, total energy contents were overestimated by much more than an order of magnitude in regions with emissions dominated by strongly aged electron spectra.

4. If sources are well resolved, it may be practical to examine correlations between the radio and X-ray intensity distributions as a probe of dynamical relationships between the particles and the magnetic field. In our synthetic observation analysis of these distributions in the simulated objects we were able to recover correctly the physical correlation between magnetic field and plasma density present in the objects.
5. In regions with very large intensity contrasts, such as near a bright hotspot, smoothing at low resolution naturally leads to biases of the inferred properties in the direction of those physically in the dominant emission regions.

Finally, a note on relativistic effects. Our surface brightness computations would have to be modified in order to obtain meaningful numbers for the case of relativistic flows. However, our main purpose has not been to study the details of the surface brightness distributions so much as it has been to try to understand how well we recover meaningful information from the observations if we model them in simple but appropriate ways. It is difficult and probably of only limited usefulness to attempt a direct comparison to the relativistic case without genuine calculations. A valuable extension of this work would be to apply the same kind of analysis to appropriately-modeled emission (i.e., including beaming and boosting effects) from relativistic flows.

The work by I. L. T. and T. W. J. was supported by the NSF under grants AST96-16964 and AST00-71176 and by the University of Minnesota Supercomputing Institute. The work by D.R. was supported in part by KOSEF through grant R01-1999-00023. We gratefully acknowledge Larry Rudnick for many helpful comments and discussions, the assistance of William Ryan in developing data analysis tools, and the anonymous referee for numerous valuable suggestions. The Los Alamos National Laboratory strongly supports academic freedom and a researcher's right to publish; therefore, the Laboratory as an institution does not endorse the viewpoint of a publication or guarantee its technical correctness.

A. CALCULATION OF OMNIDIRECTIONAL SYNCHROTRON FLUX

Assuming an isotropic emissivity, $j_{s,\nu} \equiv j_s(\nu)$, and an optically thin intervening plasma, the omnidirectional synchrotron flux at a given position, $\Phi_\nu^S(\mathbf{x})$, is estimated as

$$\Phi_\nu^S(\mathbf{x}) = \frac{1}{4\pi} \int \frac{j_{s,\nu}(\mathbf{x}')}{(\mathbf{x} - \mathbf{x}')^2} d^3\mathbf{x}'. \quad (\text{A1})$$

On a uniform grid of zone size Δ , the above equation is written as

$$\Phi_\nu^S(l, m, n) = \frac{\Delta}{4\pi} \sum_{l'=0}^{L-1} \sum_{m'=0}^{M-1} \sum_{n'=0}^{N-1} G(l - l', m - m', n - n') j_{s,\nu}(l', m', n'), \quad (\text{A2})$$

where

$$G(l - l', m - m', n - n') \equiv \frac{1}{(l - l')^2 + (m - m')^2 + (n - n')^2}. \quad (\text{A3})$$

Here, L , M , and N are the numbers of grid zones along the x , y , and z -directions, respectively. Then, from the convolution theorem, the omnidirectional flux can be computed as

$$\Phi_\nu^S(l, m, n) = \frac{\Delta}{4\pi} \mathcal{F}^{-1} \left[\hat{G}^k(p, q, r) \hat{j}_{s,\nu}^k(p, q, r) \right], \quad (\text{A4})$$

where $\hat{G}^k(p, q, r)$ and $\hat{j}_{s,\nu}^k(p, q, r)$ are the Fourier transform of $G(l, m, n)$ and $j_{s,\nu}(l, m, n)$, respectively, and \mathcal{F}^{-1} denotes the inverse Fourier transform. For $\hat{G}^k(p, q, r)$, we use

$$\hat{G}^k(p, q, r) = \frac{2\pi^2}{[\sin^2(2\pi p/L) + \sin^2(2\pi q/M) + \sin^2(2\pi r/N)]^{1/2}}. \quad (\text{A5})$$

We note that the discrete Fourier transform can be used only with a periodic grid, while ours is not. However, as described, for instance, in Binney & Tremaine (1987), we can make $G(l, m, n)$ and $j_{s,\nu}(l, m, n)$ periodic by doubling our grid along each direction (that is, by extending the range of the summation into $-L$, $-M$, and $-N$ in equation A2). However, since the synchrotron emissions are generally confined well inside the computational grid, aliasing is not significant. We have established empirically that there was little difference between using the doubled grid and using the original grid with periodic extensions.

REFERENCES

- Bagchi, J., Pislár, V., & Neto, G. B. L. 1998, MNRAS, 296, L23
- Binney, J. & Tremaine, S. 1987, Galactic Dynamics (Princeton: Princeton University Press)
- Brunetti, G., Bondi, M., Comastri, A., & Setti, G. 2002, A&A, 381, 795
- Brunetti, G., Cappi, M., Setti, G., Feretti, L., & Harris, D. E. 2001, A&A, 372, 755
- Brunetti, G., Comastri, A., Setti, G., & Feretti, L. 1999, A&A, 342, 57
- Celotti, A., Ghisellini, G., & Chiaberge, M. 2001, MNRAS, 321, L1
- Cooke, B. A., Lawrence, A., & Perola, G. C. 1978, MNRAS, 182, 661
- Crawford, C. S. & Fabian, A. C. 2003, MNRAS, 339, 1163
- Dai, W. & Woodward, P. R. 1998, ApJ, 494, 317
- Donahue, M., Daly, R. A., & Horner, D. J. 2003, ApJ, 584, 643
- Fabbiano, G., Doxsey, R. E., Johnston, M., Schwartz, D. A., & Shwarz, J. 1979, ApJ, 230, L67
- Feigelson, E. D., Laurant-Muehleisen, S. A., Kollgaard, R. I., & Fomalont, E. B. 1995, ApJ, 449, L149
- Gooch, R. E. 1995, in ASP Conf. Ser. 101, Astronomical Data Analysis Software and Systems V, ed. G. H. Jacoby & J. Barnes (San Francisco: ASP), 80
- Gregori, G., Miniati, F., Ryu, D., & Jones, T. W. 2000, ApJ, 543, 775
- Hardcastle, M. J., Birkinshaw, M., Cameron, R. A., Harris, D. E., Looney, L. W., & Worrall, D. M. 2002, ApJ, 581, 948
- Hardcastle, M. J., Birkinshaw, M., & Worrall, D. M. 2001, MNRAS, 323, L17
- Harris, D. E., Carilli, C. L., & Perley, R. A. 1994, Nature, 367, 713
- Harris, D. E. & Grindlay, J. E. 1979, MNRAS, 188, 25
- Harris, D. E., et al. 2000, ApJ, 530, L81
- Harris, D. E. & Romanishin, W. 1974, ApJ, 188, 209

- Harten, A. 1983, *J. Comp. Phys.*, 49, 357
- Jones, T. W., O’Dell, S. L., & Stein, W. A. 1974, *ApJ*, 188, 353
- Jones, T. W., Ryu, D., & Engel, A. 1999, *ApJ*, 512, 105, (JRE99)
- Kaneda, H., Tashiro, M., Ikebe, Y., Ishisaki, Y., Kubo, H., Makishima, M., Ohashi, T., Saito, Y., Tabara, H., & Takahashi, T. 1995, *ApJ*, 453, L13
- Kang, H., Jones, T. W., & Gieseler, U. D. J. 2002, *ApJ*, 579, 337
- Miley, G. 1980, *ARA&A*, Vol. 18 (Annual Reviews, Inc.), 165
- Röser, H.-J., Meisenheimer, K., Neumann, M., Conway, R. G., & Perley, R. A. 2000, *A&A*, 360, 99
- Ryu, D. & Jones, T. W. 1995, *ApJ*, 442, 228
- Ryu, D., Jones, T. W., & Frank, A. 1995, *ApJ*, 452, 785
- Ryu, D., Miniati, F., Jones, T. W., & Frank, A. 1998, *ApJ*, 509, 244
- Sambruna, R. M., Urry, C. M., Tavecchio, F., Maraschi, L., Scarpa, R., Chartas, G., & Muxlow, T. 2001, *ApJ*, 549, L161
- Schwartz, D. A., Marshall, H. L., Lovell, J. E. J., Piner, B. G., & Tingay, S. J. 2000, *ApJ*, 540, L69
- Setti, G., Brunetti, G., & Comastri, A. 2002, in *IAU Symposium Series*, Vol. 199, *The Universe at Low Radio Frequencies*, IAU (Astronomical Society of the Pacific), astro-ph/0002225
- Tashiro, M., Kaneda, H., Makishima, M., Iyomoto, N., Idesawa, E., Ishisaki, Y., Kotani, T., Takahashi, T., & Yamashita, Y. 1998, *ApJ*, 499, 713
- Tavecchio, F., Maraschi, L., Sambruna, R. M., & Urry, C. M. 2000, *ApJ*, 544, L23
- Tregillis, I. L. 2002, PhD thesis, University of Minnesota
- Tregillis, I. L., Jones, T. W., & Ryu, D. 2001a, in *Similarities and Universality in Relativistic Flows*, ed. M. Georganopoulos, A. Guthmann, K. Manolakou, & A. Marcowith (Berlin: Logos Verlag Berlin), 51
- Tregillis, I. L., Jones, T. W., & Ryu, D. 2001b, *ApJ*, 557, 475

- Tregillis, I. L., Jones, T. W., & Ryu, D. 2002a, in ASP Conference Series, Vol. 250, *Particles and Fields in Radio Galaxies*, ed. R. A. Laing & K. M. Blundell (San Francisco: ASP), 336
- Tregillis, I. L., Jones, T. W., Ryu, D., & Park, C. 2002b, in *Life Cycles of Radio Galaxies*, ed. J. Biretta, A. M. Koekemoer, E. S. Perlman, & C. P. O’Dea, Vol. 46 (Amsterdam: New Astronomy Reviews), 387
- Wilson, A. S., Young, A. J., & Shopbell, P. L. 2001, *ApJ*, 547, 740

Table 1: Summary of Simulations

Model ^a	ID	In-flowing Electrons ^b (b_1)	Shock Injection Parameter (ϵ)	Cooling Time ^c (Myr)	B_{x0} (μG)
1.....	Control	10^{-4}	0.0	1.63×10^4	0.39
2.....	Injection	10^{-8}	10^{-4}	1.63×10^4	0.39
3.....	Cooling	10^{-4}	0.0	54	5.7

^aAll models used external Mach 80 jets ($M_j = u_j/c_a = 80$), corresponding to a velocity of 0.05 c, and a density contrast $\eta = \rho_j/\rho_a = 0.01$; the internal jet Mach number is 8. Units derive from $r_j = 1$ (representing 2 kpc), an ambient density, $\rho_a = 1$, and a background sound speed, $c_a = (\gamma P_a/\rho_a)^{1/2} = 1$ ($\gamma = 5/3$). The initial axial magnetic field was B_{x0} ($\beta = P_a/P_b = 100$) in the ambient medium. The jet also carried an additional toroidal field component, $B_\phi = 2 \times B_{x0}(r/r_j)$. The spectrum of nonthermal electrons entering with the jet was a power-law with momentum slope $q = 4.4$, corresponding to a synchrotron spectral index $\alpha = 0.7$. The nonthermal particle distribution was specified by $N = 8$ momentum bins in all three models.

^bRatio of nonthermal to thermal electron density in the incident jet flow.

^cTime for electrons to cool below momentum $\hat{p} = 10^4 m_e c$ in the background magnetic field B_{x0} . In these simulations the time unit r_j/c_a corresponds in physical units to approximately 10 Myr.

Table 2: B_{ic} and B_{me} Along LOS 1-6

		Control Model (1)			LOS		
Field ^a	Beam ^b	1	2	3	4	5	6
B_{peak}	...	0.56	1.7	0.88	0.49	0.82	0.79
B_{rms}	...	0.24	0.45	0.30	0.17	0.35	0.30
B_{ic} ^d	0.28 ^c	0.15	1.1	0.39	0.094	0.43	0.31
	3.0	0.13	0.91	0.40	0.088	0.43	0.31
	22.0	0.18	0.37	0.34	0.19	0.36	0.29
B_{me} ^e	0.28	0.37	1.1	0.64	0.20	0.68	0.58
	3.0	0.30	0.91	0.65	0.19	0.70	0.58
	22.0	0.31	0.45	0.45	0.36	0.46	0.44
		Injection Model (2)			LOS		
Field ^a	Beam ^b	1	2	3	4	5	6
B_{peak}	...	0.56	1.7	0.88	0.49	0.82	0.79
B_{rms}	...	0.24	0.45	0.30	0.17	0.35	0.30
B_{ic} ^d	0.28 ^c	0.068	0.65	0.23	0.077	0.15	0.30
	3.0	0.052	0.69	0.89	0.087	1.5	0.29
	22.0	0.95	0.89	1.2	0.15	1.1	0.16
B_{me} ^e	0.28	0.044	0.42	0.077	0.020	0.050	0.044
	3.0	0.049	0.39	0.11	0.023	0.39	0.060
	22.0	0.13	0.23	0.23	0.037	0.24	0.13
		Cooling Model (3)			LOS		
Field ^a	Beam ^b	1	2	3	4	5	6
B_{peak}	...	8.3	25.3	13.1	7.3	12.1	11.7
B_{rms}	...	3.5	6.7	4.5	2.6	5.3	4.5
B_{ic} ^d	0.28 ^c	2.3	22.6	6.5	7.9	8.1	4.6
	3.0	2.8	17.3	6.5	5.5	8.0	4.8
	22.0	4.0	7.0	5.6	8.3	6.2	2.4
B_{me} ^e	0.28	15.3	24.2	14.2	242	16.6	10.2
	3.0	12.2	17.3	11.0	29.8	12.3	8.8
	22.0	5.2	8.5	7.7	5.5	8.1	4.4

^aAll magnetic field values listed in μG .

^bFWHM of convolved Gaussian in arcseconds.

^cUnconvolved pixel size in arcseconds.

^dCalculated from radio observation at 2.9 GHz and X-ray observation at 1.2 keV.

^eCalculated using commonly-assumed $k = \eta = \sin \vartheta = 1$. Upper and lower cutoff frequencies are known from the model parameters. For Models **1** and **2**, $\nu_1 = 100$ Hz and $\nu_2 = 30$ GHz. For Model **3**, $\nu_1 = 1500$ Hz and $\nu_2 = 450$ GHz. Calculation is based on synthetic radio surface brightness map at 2.9GHz.

Table 3: Energy Partitioning Along LOS 1-6

Model	ID	LOS	d_{rms}	$\langle d \rangle$	$d_{obs} = 1.5 \left(\frac{B_{ic}}{B_{me}} \right)^{7/2}$ ^a
1	Control ^b	1	0.351	0.280	6.36×10^{-2}
		2	0.213	0.173	1.50
		3	0.311	0.239	0.265
		4	0.756	0.432	0.107
		5	0.268	0.247	0.302
		6	0.797	0.364	0.167
2	Injection ^c	1	148	96.2	6.88
		2	285	129	6.92
		3	1110	716	69.1
		4	821	479	168
		5	1070	707	70.1
		6	4340	1970	1240
3	Cooling ^b	1	0.278	0.217	1.98×10^{-3}
		2	0.783	0.539	1.18
		3	0.584	0.373	9.73×10^{-2}
		4	0.192	0.141	9.43×10^{-6}
		5	0.276	0.226	0.122
		6	1.170	0.413	9.24×10^{-2}

^a d_{obs} found from equation (9) with $B = B_{ic}$ and $k = 1$.

^bInflow boundary conditions set $d_0 = 0.16$ in the jet for these models.

^cInflow boundary conditions set $d_0 = 1600$ in the jet for this model.

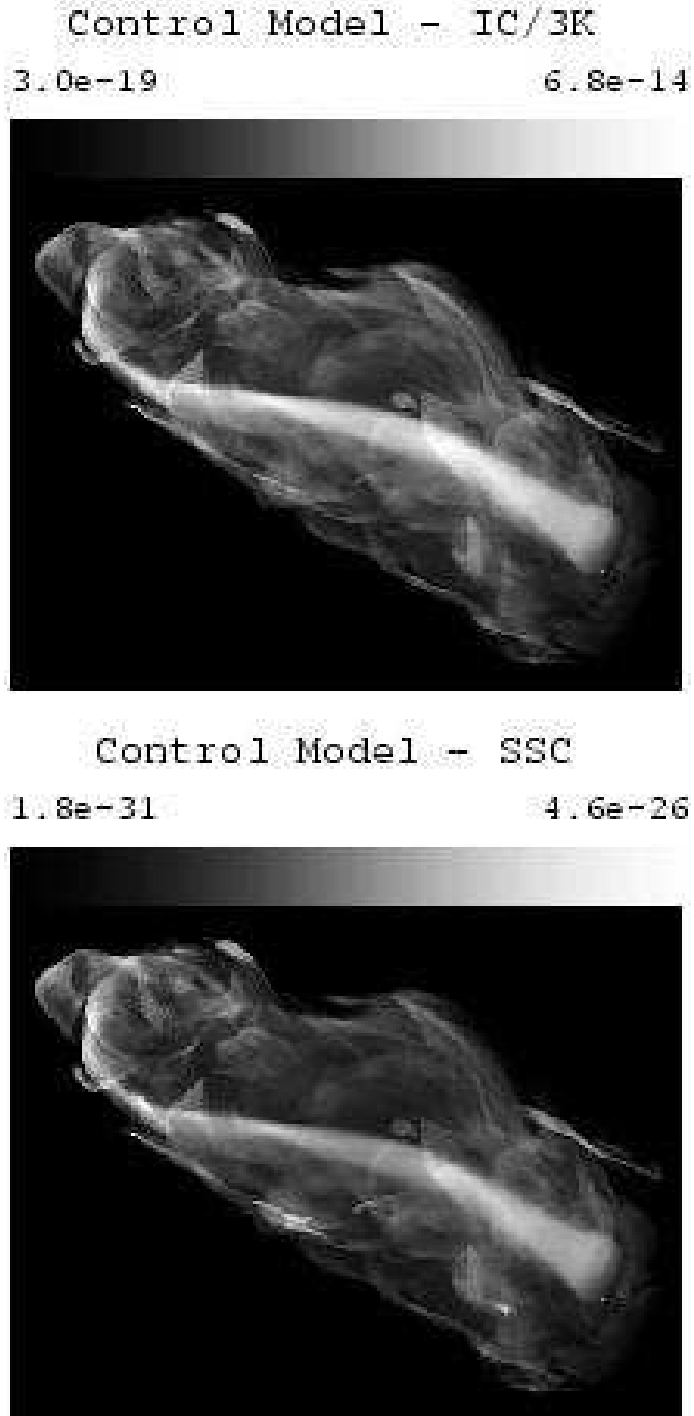


Fig. 1.— 1.2 keV X-ray surface brightness maps for the Control Model. Both images are displayed using a square-root transfer function. The brightness limits are in code units.

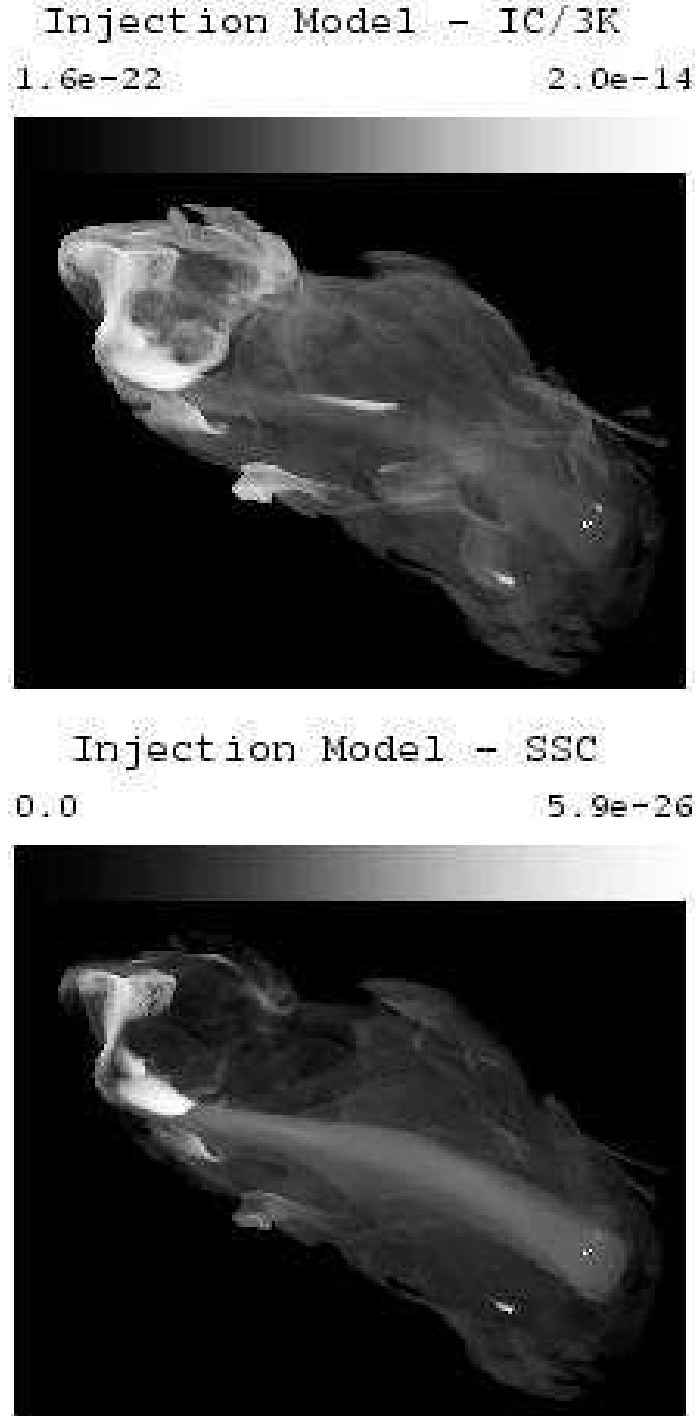


Fig. 2.— 1.2 keV X-ray surface brightness maps for the Injection Model. Both images are displayed using a logarithmic transfer function. The brightness limits are in code units.

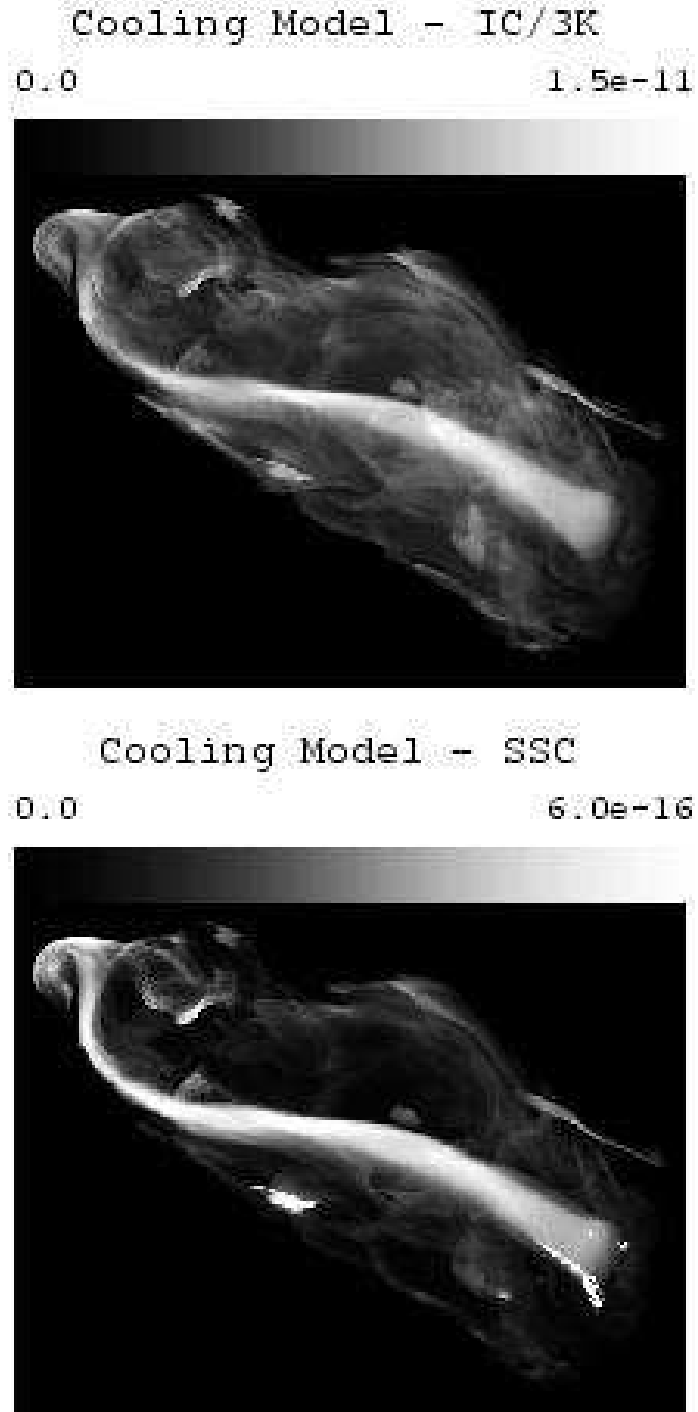


Fig. 3.— 1.2 keV X-ray surface brightness maps for the Cooling Model. Both images are displayed using a square-root transfer function. The brightness limits are in code units.

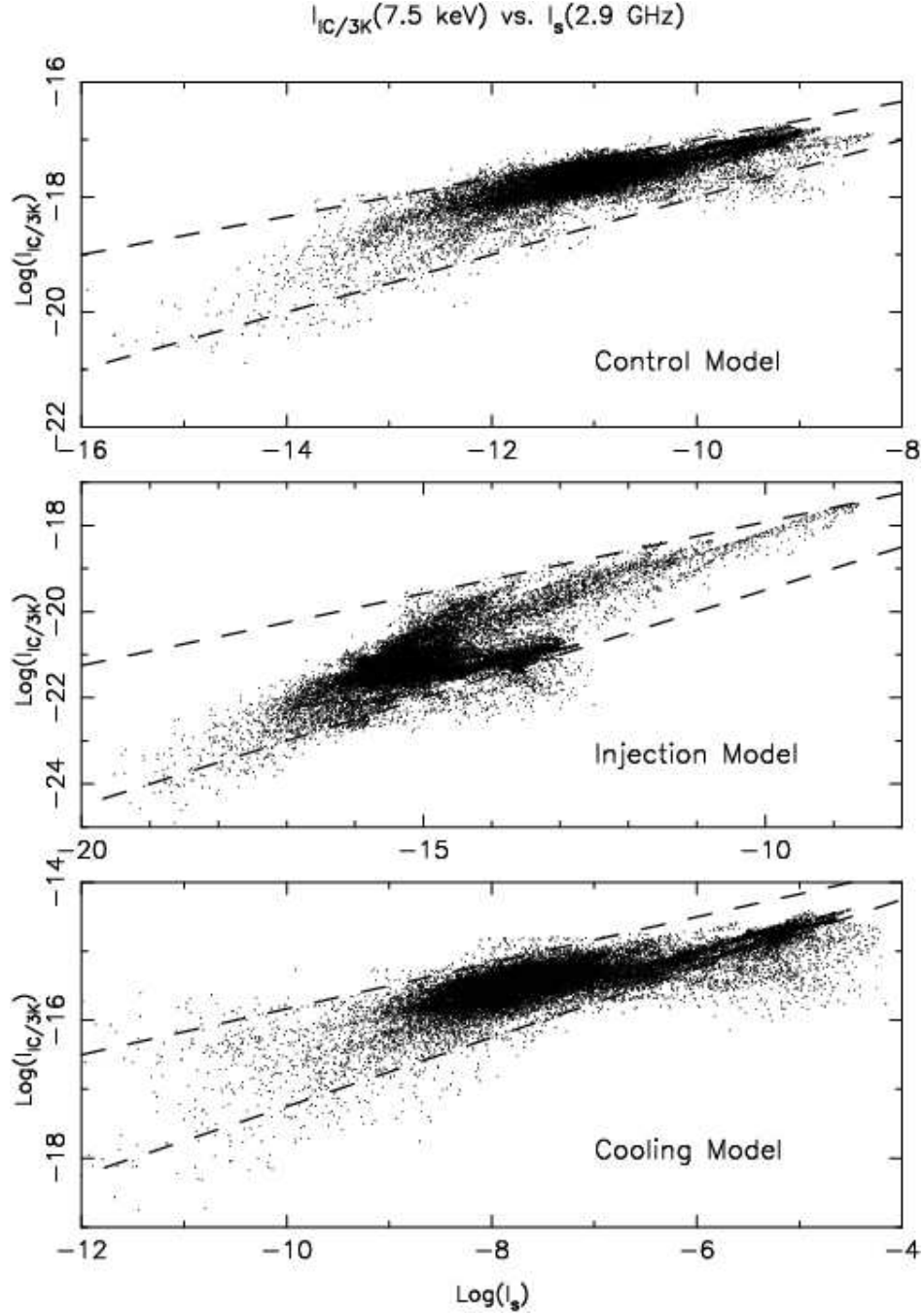


Fig. 4.— Scatterplots of 7.5 keV IC/3K vs. 2.9 GHz synchrotron brightness in code units for each electron transport model. In each model, the radio hotspot is represented by the diffuse collection of points at the highest radio brightnesses. In the Injection Model the hotspot is very prominent because it is significantly brighter than the jet. The brightest portions of the jet in the Control Model and Cooling Model are represented by the densest collection of points just below the hotspot in radio brightness. The dashed lines represent the relationships $I_{\text{IC/3K}} \propto I_s^{1/3}$ and $I_{\text{IC/3K}} \propto I_s^{1/2}$. They are solely for comparison and are not statistical fits.

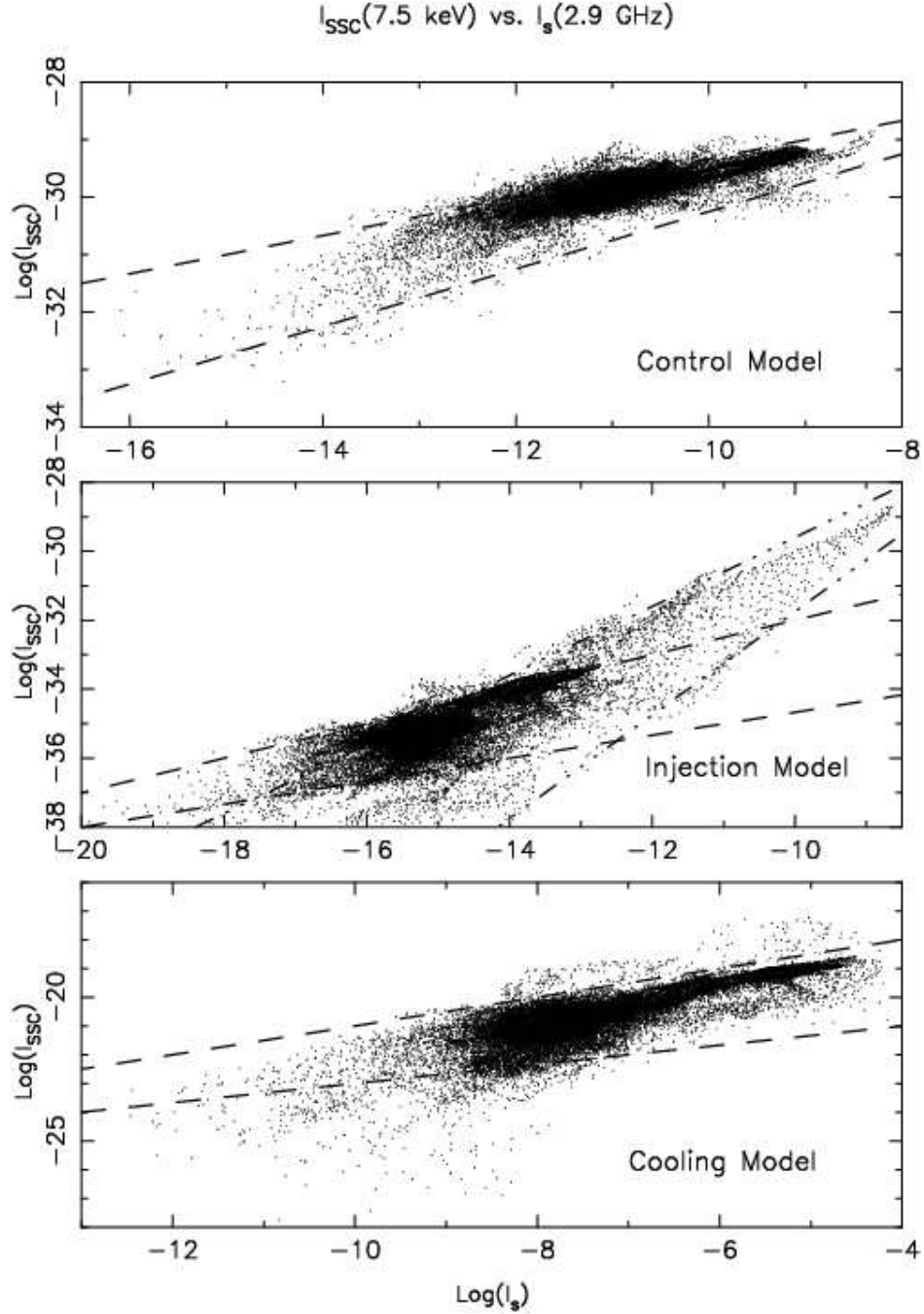


Fig. 5.— Scatterplots of 7.5 keV SSC vs. 2.9 GHz synchrotron brightness in code units. For numerical reasons, the minimum (log) SSC X-ray brightness is fixed at -38. In each model the hotspot is represented by the diffuse collection of points at the highest radio brightnesses. The Injection Model hotspot is clearly visible. In the Control Model and Cooling Model the radio hotspot is not much brighter than the surrounding jet material, represented by the dense collection of points at slightly lower brightnesses. The dashed lines represent the relationships $I_{SSC} \propto I_s^{1/3}$ and $I_{SSC} \propto I_s^{1/2}$. The dot-dashed lines represent the relationships $I_{SSC} \propto I_s^{1.0}$ and $I_{SSC} \propto I_s^{1.5}$. All lines are solely for comparison and are not statistical fits.

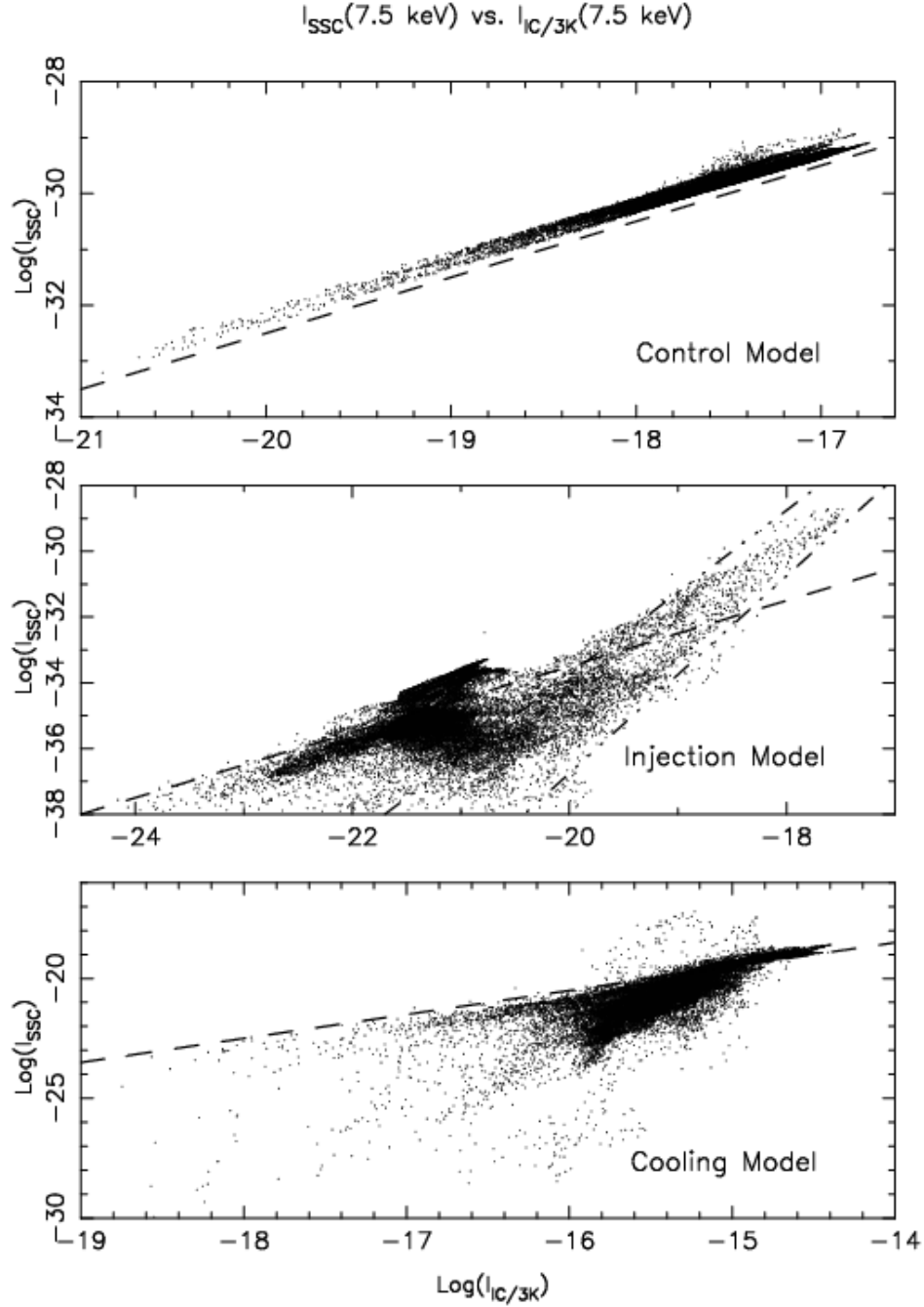


Fig. 6.— Scatterplots of 7.5 keV SSC vs. 7.5 keV IC/3K brightness. In the Control and Cooling Models, the highest SSC and IC/3K brightnesses generally correspond to the radio hotspot, contributing to the tight correlation between the highest X-ray brightnesses. The Injection Model hotspot is again quite prominent. The dashed lines represent the relationship $I_{\text{SSC}} \propto I_{\text{IC/3K}}^{1.0}$. The dot-dashed lines represent the relationships $I_{\text{SSC}} \propto I_{\text{IC/3K}}^{2.5}$ and $I_{\text{SSC}} \propto I_{\text{IC/3K}}^{3.0}$. All lines are solely for comparison and are not statistical fits.

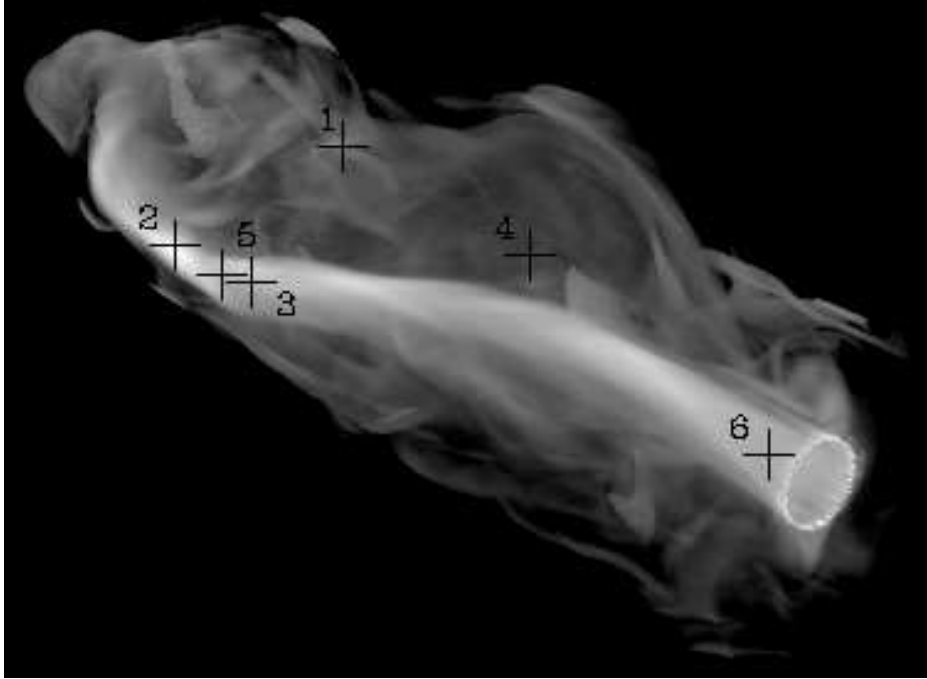


Fig. 7.— Greyscale image of the Control Model 8 GHz synchrotron surface brightness. The 6 crosses denote the lines of sight (LOS) used for analysis of the IC/3K and energy partitioning in §§4-5.

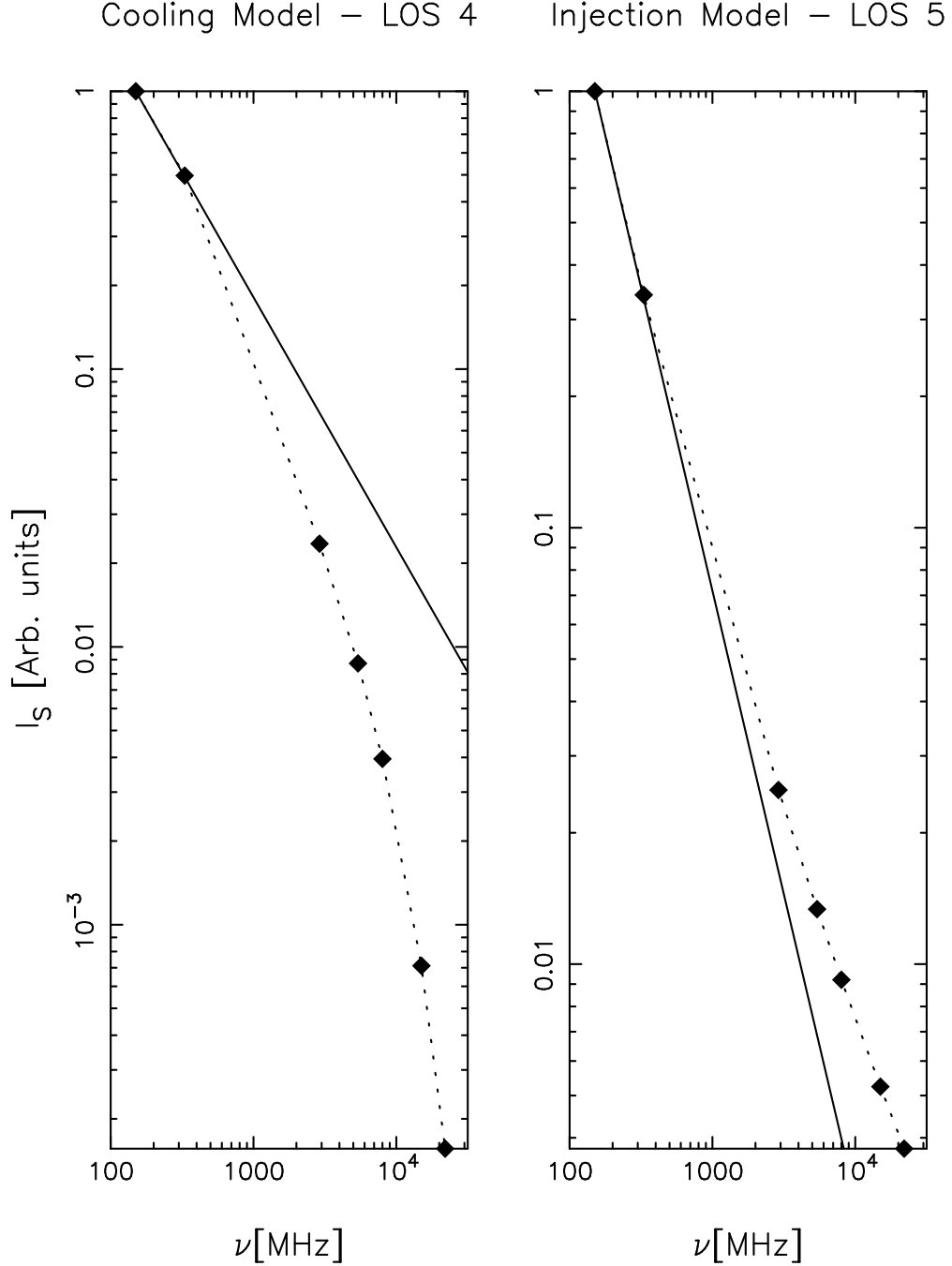


Fig. 8.— Synchrotron spectra at **LOS 4** in the Cooling Model and **LOS 5** in the Injection Model. Both spectra are comprised of synthetic surface brightness calculations at 150 MHz, 330 MHz, 2.9 GHz, 5.4 GHz, 8.0 GHz, 15.0 GHz, and 22.0 GHz. The spectra have been scaled so that the surface brightness is equal to unity at the lowest frequency. For reference, we have included a power-law line with $\alpha = 0.90$ in the left panel, and a power-law line with $\alpha = 1.39$ in the right panel. Note that in both cases, significant deviations from the power-law form are apparent at frequencies as low as 2.9 GHz.

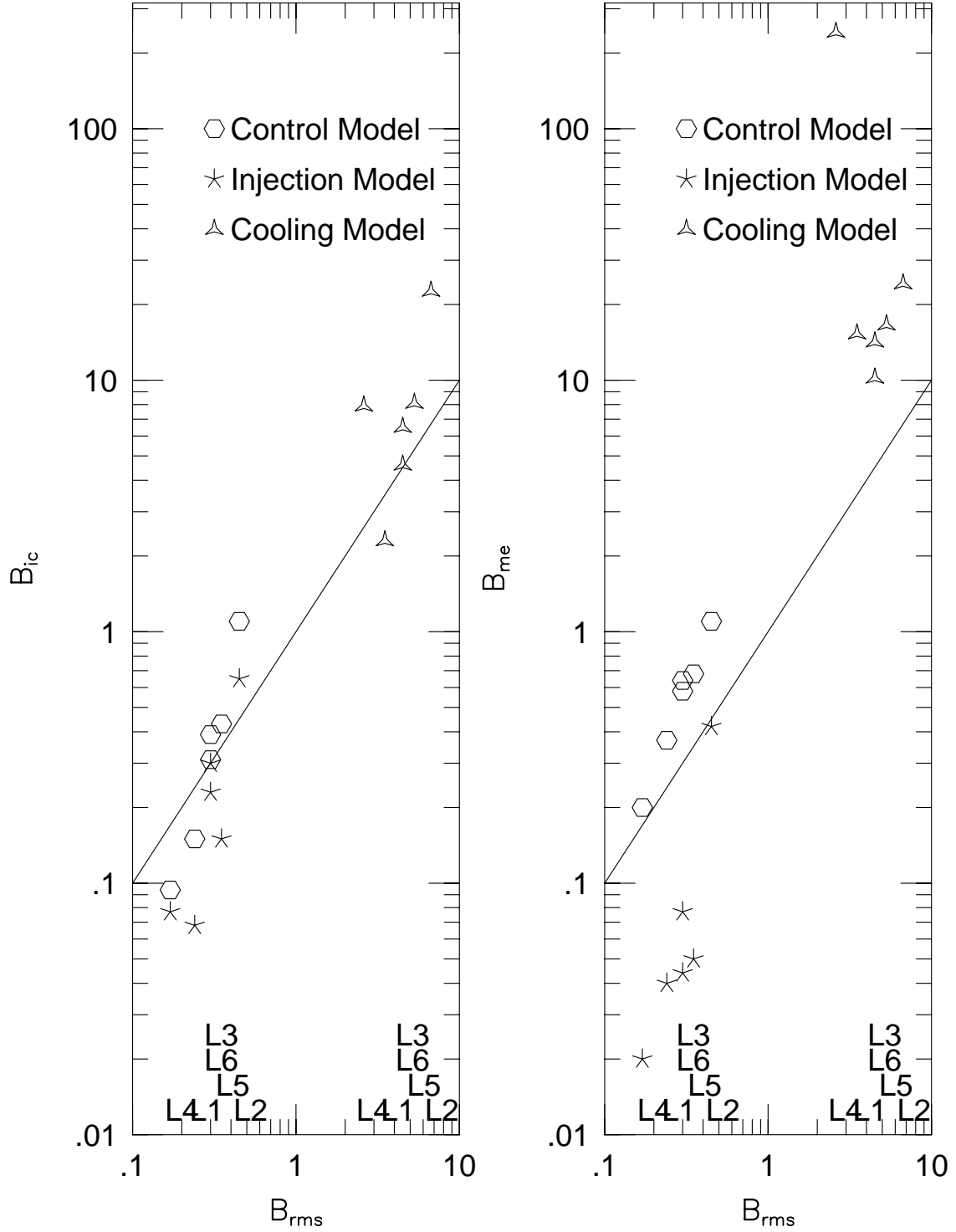


Fig. 9.— Comparisons of magnetic field measures from Table 2. Symbols indicate the electron transport model. Associated LOS numbers are marked at the bottom of each plot according to the associated B_{rms} values.

Magnetic Field along LOS for Control and Injection Models

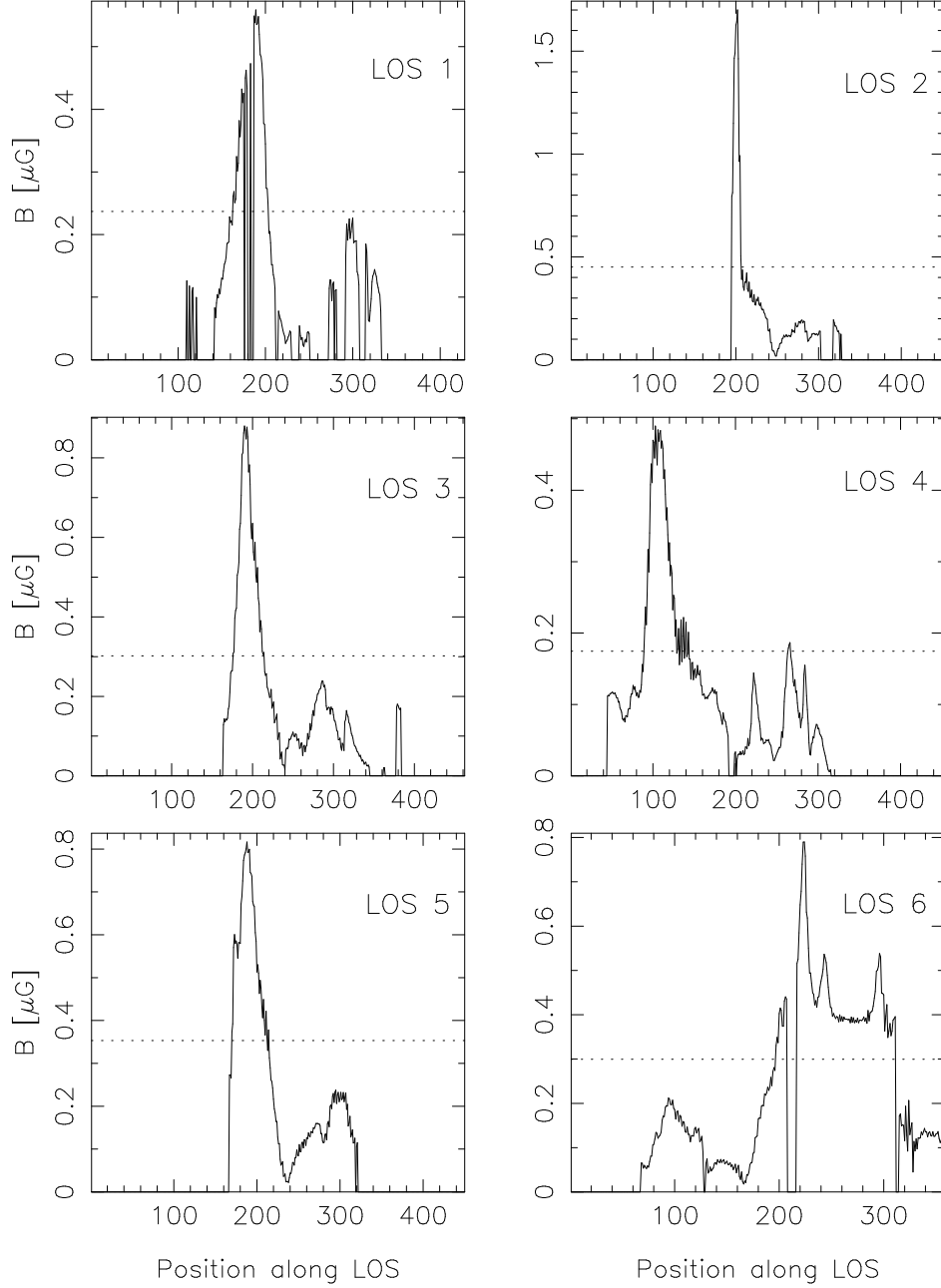


Fig. 10.— Physical magnetic field values along **LOS 1-6** marked in Figure 7 for the Control Model and Injection Model. For the Cooling Model increase each field point by a factor 14.6. Wherever the jet mass fraction (“color”) is less than 99% the fields have been filtered out. On each LOS the filtered RMS field is marked with a dotted line; the RMS values are listed in table 2. The distance unit is computational zones along the LOS. Low values correspond to the side of the source closer to the hypothetical observer.

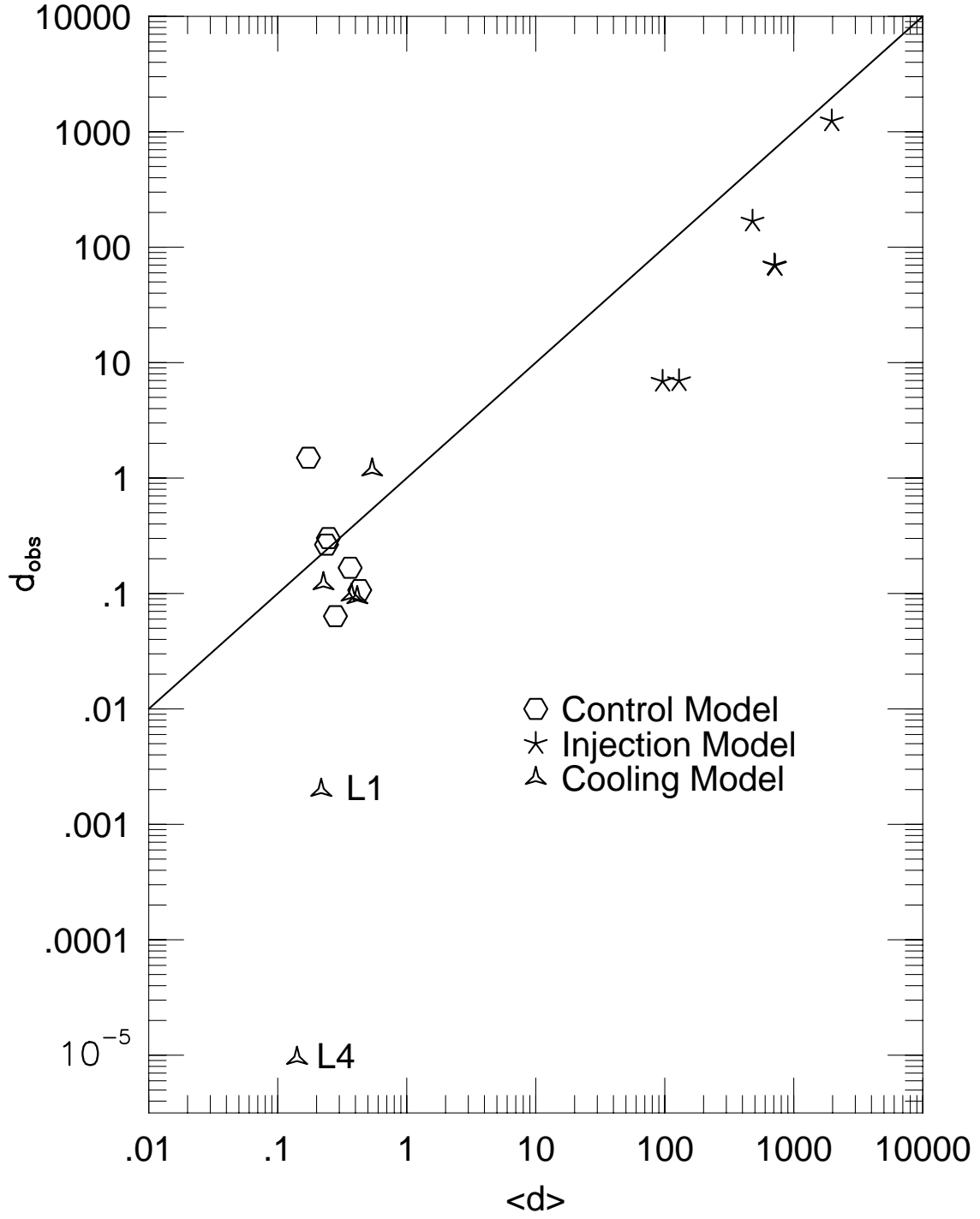


Fig. 11.— Comparisons of d_{obs} and $\langle d \rangle$ from Table 3. Symbols indicate the associated electron transport model.

Energy Partitioning Along LOS for Control Model

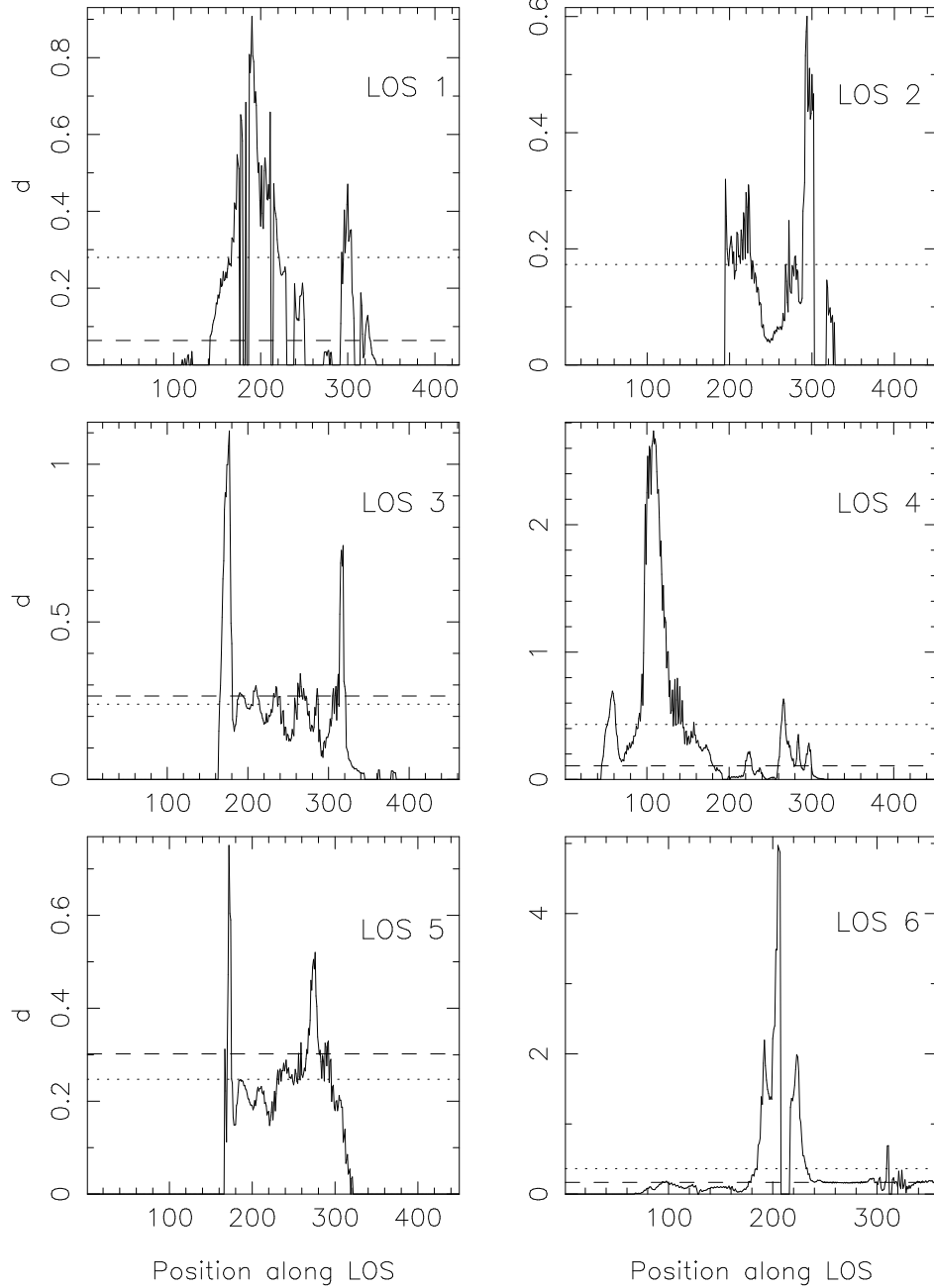


Fig. 12.— Parameter d along **LOS 1-6** for the Control Model. The average $\langle d \rangle$ is marked by a dotted line, and the “observed” value from equation (9) with $B = B_{ic}$ is marked with a dashed line. For reference, on axis the in-flowing jet carries $d_0 = 0.16$. Distance refers to computational zones along the LOS. Low values correspond to the side of the source closer to the hypothetical observer.

Energy Partitioning Along LOS for Injection Model

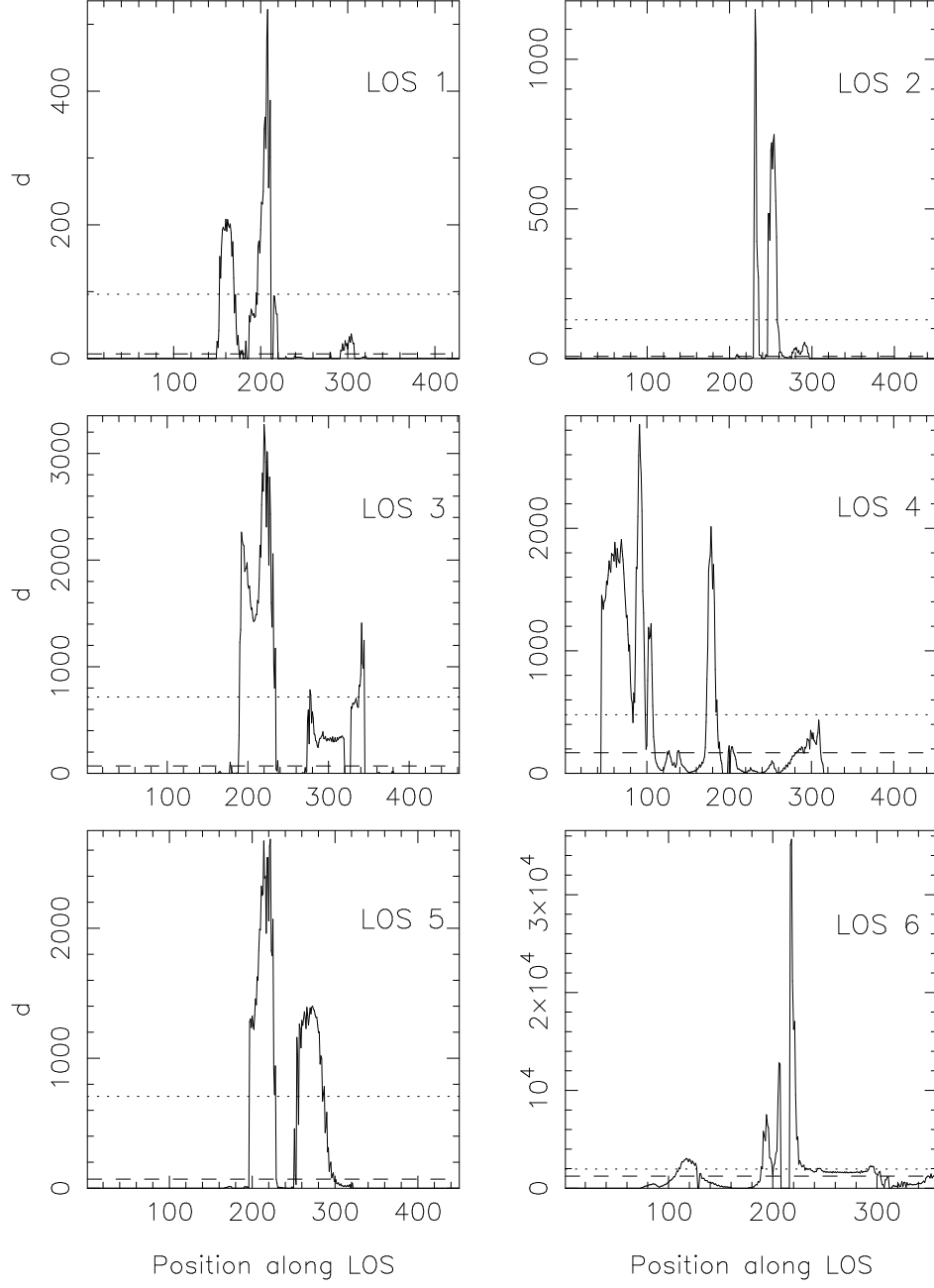


Fig. 13.— Same as Figure 12 for the Injection Model. For reference, on axis the in-flowing jet carries $d_0 = 1600$.

Energy Partitioning Along LOS for Cooling Model

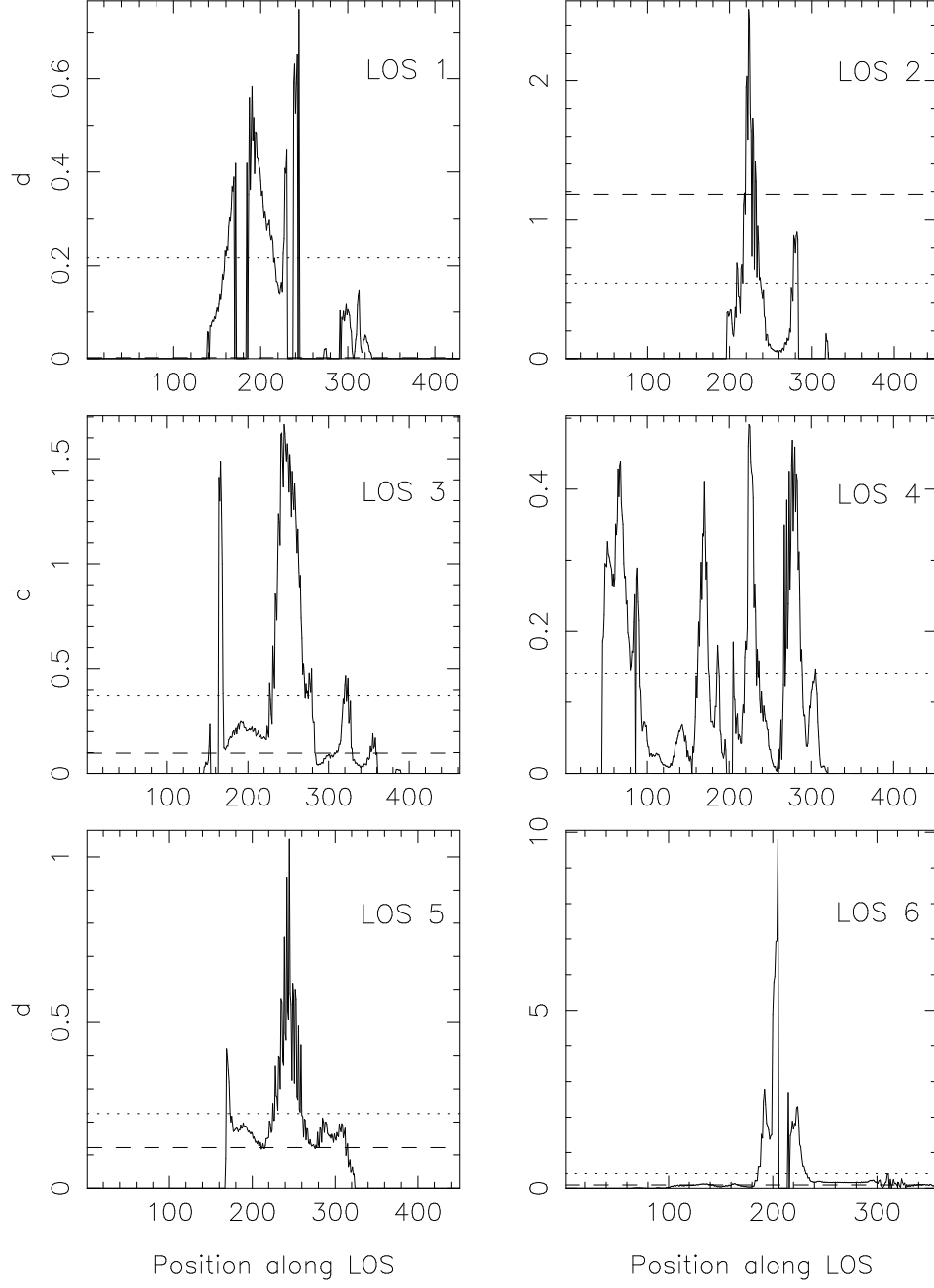


Fig. 14.— Same as Figure 12 for the Cooling Model. For reference, on axis the in-flowing jet carries $d_0 = 0.16$.